A TRMM Microwave Radiometer Rain Rate Estimation Method with Convective and Stratiform Discrimination

C. Prabhakara[1], R. Iacovazzi, Jr.[2], J. A. Weinman[1], and G. Dalu[3]

[1]NASA/Goddard Space Flight Center
[2]Raytheon ITSS Corporation
[3]CNR, Italy

Submitted to

Journal of the Meteorological Society of Japan

Corresponding Author Address

C. Prabhakara
NASA/Goddard Space Flight Center, Code 913
Greenbelt, Maryland 20771
Phone : 301-614-6193; Fax : 301-614-6307; E-mail : cuddapah@climate.gsfc.nasa.gov

Abstract

Tropical Rainfall Measuring Mission (TRMM) Microwave Imager (TMI) radiometer brightness temperature data in the 85 GHz channel (T85) reveal distinct local minima ($T85_{min}$) in a regional map containing a Mesoscale Convective System (MCS). This is because of relatively small footprint size (~ 5.5 km) and strong extinction properties in this channel of the TMI. A map of surface rain rate for that region, deduced from simultaneous measurements made by the Precipitation Radar (PR) on board the TRMM satellite, reveals that these $T85_{min}$, produced by scattering, correspond to local PR rain maxima. Utilizing the PR rain rate map as a guide, we infer empirically from TMI data the presence of three different kinds of thunderstorms or Cbs. These Cbs are classified as young, mature, and decaying types, and are assumed to have a scale of about 20 km on the average. Two parameters are used to classify these three kinds of Cbs based on the T85 data: a) the magnitude of scattering depression deduced from local $T85_{min}$ and b) the mean horizontal gradient of T85 around such minima. Knowing the category of a given Cb, we can estimate the rain rate associated with it. Such estimation is done with the help of relationships linking $T85_{min}$ to rain rate in each Cb type. Similarly, a weak background rain rate in all the areas where T85 is less than 260 K is deduced with another relationship linking T85 to rain rate. In our rain retrieval model, this background rain constitutes stratiform rain where the Cbs are absent. Initially, these relationships are optimized or tuned utilizing the PR and TMI data of a few MCS events. After such tuning, the model is applied to independent MCS cases. The areal distribution of light (1-10 $mmhr^{-1}$), moderate (10-20 $mmhr^{-1}$), and intense ($\geq$ 20 $mmhr^{-1}$) rain rates are retrieved satisfactorily. Accuracy in the estimates of the light, moderate, and intense rain areas and the mean rain rates associated with such areas in these independent MCS cases is on the average about 15 %. Taking

advantage of this ability of our retrieval method, one could derive the latent heat input into the atmosphere over the 760 km wide swath of the TMI radiometer in the tropics.

1. Introduction

Several microwave radiative-transfer rain retrieval models (see for e.g. Wu and Weinman, 1984; Kummerow et al., 1989; Smith and Mugnai, 1992; and Prabhakara et al., 1995) have taken into consideration microwave scattering by dense solid ice particles, which are generally associated with convective clouds. However, Schols et al. (1999) indicate that in order to explain satellite-borne Special Sensor Microwave Imager (SSM/I)[1] brightness temperature data associated with stratiform precipitation produced by nimbostratus clouds, radiative properties of frozen and melting ice aggregates (snow) with low density have to be considered. Otherwise, a significant uncertainty in estimation of such stratiform rain rates from SSM/I data will result. In order to objectively sense dense ice particles (frozen rain drops and graupel) or less dense ice particles (frozen and melting ice aggregates), a spectral signature is needed from the microwave radiometer data. Such a distinct signature is missing in the limited information contained in the dual-polarization, multispectral SSM/I data (Schols et al., 1995; Prabhakara et al., 1998). This is because measurements in all the channels of this instrument have a high degree of redundancy. This lack of information in the microwave radiometer data can lead to significant errors in rain retrievals that are based solely on radiative transfer theory.

---

[1] *Radiometer of the Defense Meteorological Satellite Program (DMSP) that has 19, 37 and 85 GHz channels in dual polarization and a 22 GHz channel in vertical polarization. This radiometer observes the earth's surface and atmosphere in a conical scan with an incidence angle of ~ 50^0(for more details see Hollinger et al., 1985).*

This problem associated with retrieving rain using microwave radiative transfer models is exemplified over oceanic regions by the studies of Heymsfield et al. (1996) and McGaughey and Zipser (1996). They find from aircraft radar and microwave radiometer observations that retrievals from current models that consider dense ice particles perform poorly. Based on the Schols et al. (1999) study, we infer that this is largely due to improper specification of the nature of the ice particles in the models. We may remark that the spatial resolution of these aircraft instruments is a few kilometers, which is much smaller compared to that of the SSM/I. Crude spatial resolution of the satellite-borne microwave radiometers is often cited as the dominant reason for significant errors in rain retrievals (see for e.g. Kummerow, 1998). However, we contend, based on the errors in rain rate retrievals from SSM/I and aircraft radiometer data, that spatial resolution is not the only cause of such errors. The ability to discriminate the nature of ice hydrometeors is also an important factor.

On land regions, rain retrieval from microwave radiometer data is further complicated by variable surface emissivity introduced by vegetation, surface wetness, water bodies and terrain. Conner and Petty (1998) indicate that the spectral information contained in the SSM/I data over land can explain only about 30% of the variance present in the radar or the rain gauge observations over land. From the above discussion, we conclude that because of the spatial inhomogeneities and the uncertainties in the nature of the hydrometeors, radiative transfer models do not succeed in retrieving rain rate over land. Thus, in order to get good rain retrievals over land and ocean, more information in addition to the microwave radiometer spectral measurements is needed.

In the studies of Prabhakara et al. (1998, 1999), the rain area in a mesoscale geographic region (~ 2^{o} lat x 3^{o} lon) deduced from the SSM/I data is provided as additional information to estimate the mesoscale area-average rain rate. Those studies indicate that the rain area in a mesoscale region serves as a more important factor in estimating area-average rain rate than the spectral information given by the SSM/I data. This mesoscale area-average rain retrieval approach is widely used and has its basis in the Area Time Integral concepts of Doneaud et al. (1984) and Lopez et al. (1989). A useful inference from these studies is that the atmospheric dynamics that lead to the total volume of rain in a mesoscale region are coupled to the rain area in that region.

Based on a similar conceptual framework, in this study the spatial, and the spectral, information given by the Tropical Rainfall Measuring Mission (TRMM[2]) Microwave Imager (TMI) radiometer data are used in an empirical fashion to identify the presence of thunderstorms (Cbs) and obtain convective rain rate in the limited area of those Cbs. The rain areas outside of such limited convective regions are considered to be stratiform in nature. The empirical method developed in this study is designed to perform well over both land and ocean. Such spatial information, derived from satellite infrared radiometer observations, has been utilized empirically in an earlier study by Adler and Negri (1988) for the purpose of obtaining convective and stratiform rain. However, since microwave data represent properties of the dense layers in precipitating clouds, and not just the thin layer near

---

[2] *Tropical Rainfall Measuring Mission. On board the TRMM satellite, there is the cross-track-scanning Precipitation Radar (PR) and the conical-scanning TRMM Microwave Imager (TMI) (see Simpson et al., 1996).*

the cloud tops, microwave techniques perform better than infrared techniques in retrieving instantaneous estimates of rain rate (Ebert et al., 1996).

Hong et al. (1999) developed an empirical rain retrieval method that utilizes the spatial distribution of the SSM/I microwave radiometer measurements on ocean. This method was optimized with the help of the TOGA-COARE radar observations. In this formulation, convective/stratiform index (CSI) for each pixel is given by a combination of two quantities: 1) variability in brightness temperature near the pixel, and 2) the contrast in brightness temperature at the pixel relative to clear sky conditions. This CSI scheme of Hong et al. (1999) has difficulty to limit convective rain area to the thunderstorm scale. This scheme is used in the TRMM Project as a standard procedure to retrieve rain rates on ocean from the TMI microwave radiometer measurements. Olson et al. (1999) have considered in detail the merits of the Hong et al. (1999) rain retrievals. They find that this algorithm leads to a high bias in rain rate estimation with respect to radar, because it over estimates rain in the low to moderate range (0.1 to 16 mmhr^{-1}). Hong et al. (1999) do not demonstrate the utility of their rain retrieval formulation on land regions. The objective of this study is to improve the state-of-the-art, such that we can get quantitative convective and stratiform rain retrievals over both ocean and land.

In the TRMM mission, the TMI measurements cover a swath width of 760 km. On the other hand, the Precipitation Radar (PR) on board the TRMM satellite has a cross-track scan that covers only the 220 km central portion of the TMI swath (Simpson et al., 1996). This study aims to develop a method than can exploit this much larger scanning capability, and thereby expand temporal and spatial coverage of rain information over land and ocean regions beyond that of the PR.

2. Model to Retrieve Rain Rate Maps with Convective and Stratiform Discrimination Based on TMI data

(a) General Considerations

The TMI radiometer is similar to the SSM/I, except that it has two additional spectral channels (vertical and horizontal polarization) at 10 GHz. Furthermore, because of the lower altitude of the TRMM satellite, the spatial resolution of the TMI radiometer is about two times finer compared to SSM/I. This finer resolution, in conjunction with the spectral information, offers an opportunity to discriminate convective rain from stratiform rain.

We may remark that the vertical resolving capability of the radar gives it a distinct advantage over the passive microwave radiometer. Furthermore, radar back scatter measurements have a d^6 dependence on the rain drop diameter (Battan, 1973), while radiometer observations tend to have about a d^3 dependence (see for e.g. Olson, 1996). Both of these properties of the radar help it to isolate the rain layer and to get a more robust estimate of rain rate. However, it may be remarked that rain rate estimates based on radar data are linked to the rain drop size distribution (DSD).

There is a difference in DSD between convective and stratiform rain. Tokay and Short (1996) show with disdrometer data that the mode radius of the DSD for a given rain rate in stratiform rain is larger. This difference, if it is not accounted for, could lead to an overestimation of stratiform rain rate by about a factor of two. However, difference in DSD associated with convective and stratiform rain can be inferred with the help of horizontal inhomogeneity in rain rate (Steiner et al., 1995).

From such inference, errors in rain rate estimation can be minimized. In addition to this problem, there could be other temporal variabilities in DSD. Probable error in rain rate due to such DSD variability is estimated to be within ~ 50 %. This error estimate is based on simulations of radar backscatter using disdrometer observed DSD (R. Meneghini, personal communication). Because of these non-negligible errors, radar rain rates are calibrated with respect to surface rain gauges. An example of such calibration is that performed over Japan with the Automatic Meteorological Data Acquisition System (see for e.g. Oki et al., 1997).

Unlike radar observations, spectral information from measurements made by microwave radiometers have poor vertical resolution and ability to discriminate stratiform versus convective rain. Therefore, as shown in the study of Heymsfield et al. (1996), there are much larger errors associated with rain rates retrieved using radiometer spectral data. For these reasons, until better ground truth is available, we will use the TRMM Precipitation Radar (PR) rain estimates as a basis to develop our TMI rain retrieval method. When better ground truth is available, this TMI algorithm can be readily tuned with the help of such information.

We may point out that the current rain retrieval algorithm used to obtain the TRMM Project TMI Standard Rain Rate, R_{TMI}, on ocean is based on an empirical scheme of Hong et al. (1999). This empirical scheme is developed by a tuning procedure using SSM/I and radar observations made over TOGA-COARE. This procedure contains information from the 19 and 37 GHz channels of the radiometer, which are contaminated by surface emissivity effects on land. We contend, for this reason, that the scheme of Hong et al. is not adaptable to land regions. With the help of the radar data, in this study, we wish to develop one empirical rain retrieval scheme that is applicable to both land and ocean.

(b) Model Development

Studies of Houze and Betts (1981) and Houze (1993, 1997) show that in Mesoscale Convective Systems (MCSs) there are thunderstorms or cumulonimbus clouds (Cbs) in different stages of growth. A Cb may contain a single cloud cell or multiple cloud cells. The scale of these Cbs may vary somewhat, but on average it is about 20 km. In a gross fashion, a given Cb may be categorized as *young, mature,* or *decaying* according to its age. The young Cbs have cloud cells with moderate to strong vertical motions of several ms^{-1}, in which rain drops grow primarily through the coalescence mechanism. Because these young Cbs have not grown deep into the atmosphere, there are relatively small amounts of ice particles in these Cbs. The mature Cbs have strong vertical motions, which reach high altitudes and produce larger amounts of frozen rain drops and graupel. In the studies of Houze, moderate and intense rain rates are reflected by the strength of the narrow updrafts in the young and mature Cbs, respectively. For both the young and mature Cbs, the strength of the vertical motions and the rain rate are found to decrease rapidly toward the Cb edge. On the contrary, it is found in the decaying Cbs that the vertical motions are relatively weak (< 1 ms^{-1}), which allows sufficient time for the growth of falling ice crystals by deposition of water vapor. In turn, these ice crystals form ice aggregates before entering the melting layer, and then melt to form rain below this layer. This type of rain is stratiform in nature and relatively weak, but is more homogeneous in a given area. We take advantage of these concepts of cloud dynamics and microphysics in our empirical model, even though we do not have observations of vertical velocities and hydrometeors. The model adopted in this study to classify Cbs into the three categories, as described below, depends on T85 and its spatial distribution.

In Figure 1a, a map of a rain event over the Southeast United States on 5 June 1998 (Day 156) is depicted using the TMI T85 horizontal polarization data. The horizontal polarization is preferred because of the surface emissivity effect, which gives it a larger dynamic range over land and ocean compared to the vertical polarization data. We emphasize the 85 GHz TMI data in this study because, of all the channels of this radiometer, the 85 GHz channel has the finest spatial resolution and the highest extinction to ice and liquid hydrometeors. In particular, the scattering of microwave radiation, which according to radiative transfer theory results in a depression in the 85 GHz data, is strongly related to cloud ice content (Wu and Weinman, 1984). The surface rain rate map deduced from the PR data for the same time period (within two minutes) is shown in Figure 1b. These maps represent the 220 km central portion of the TMI swath.

The PR surface rain rate map shown in Fig. 1b has a character similar to rain maps derived from conventional radars (see for example Houze, 1993). In particular, the striking contrast between heavy rain rate in convective cells and weak rain rate present in the extensive stratiform region is faithfully reproduced in the PR data. The commonly observed log-normal type of frequency distribution of rain rate (Jones and Sims, 1978) is also revealed by the PR surface rain rates. This frequency distribution is illustrated in Figure 1c using the PR surface rain rates displayed in Fig. 1b. These properties of the PR data reinforce their credibility.

From the map of PR surface rain rate shown in Fig. 1b, we discern that there is a squall line composed of several intense Cbs. Furthermore, there are several other weaker Cbs. Some of these weaker Cbs are present in the extensive stratiform region. By comparing the PR rain rate map with the map of T85, we notice there are local minima in T85 ($T85_{min}$), which correspond roughly to rain maxima in the PR

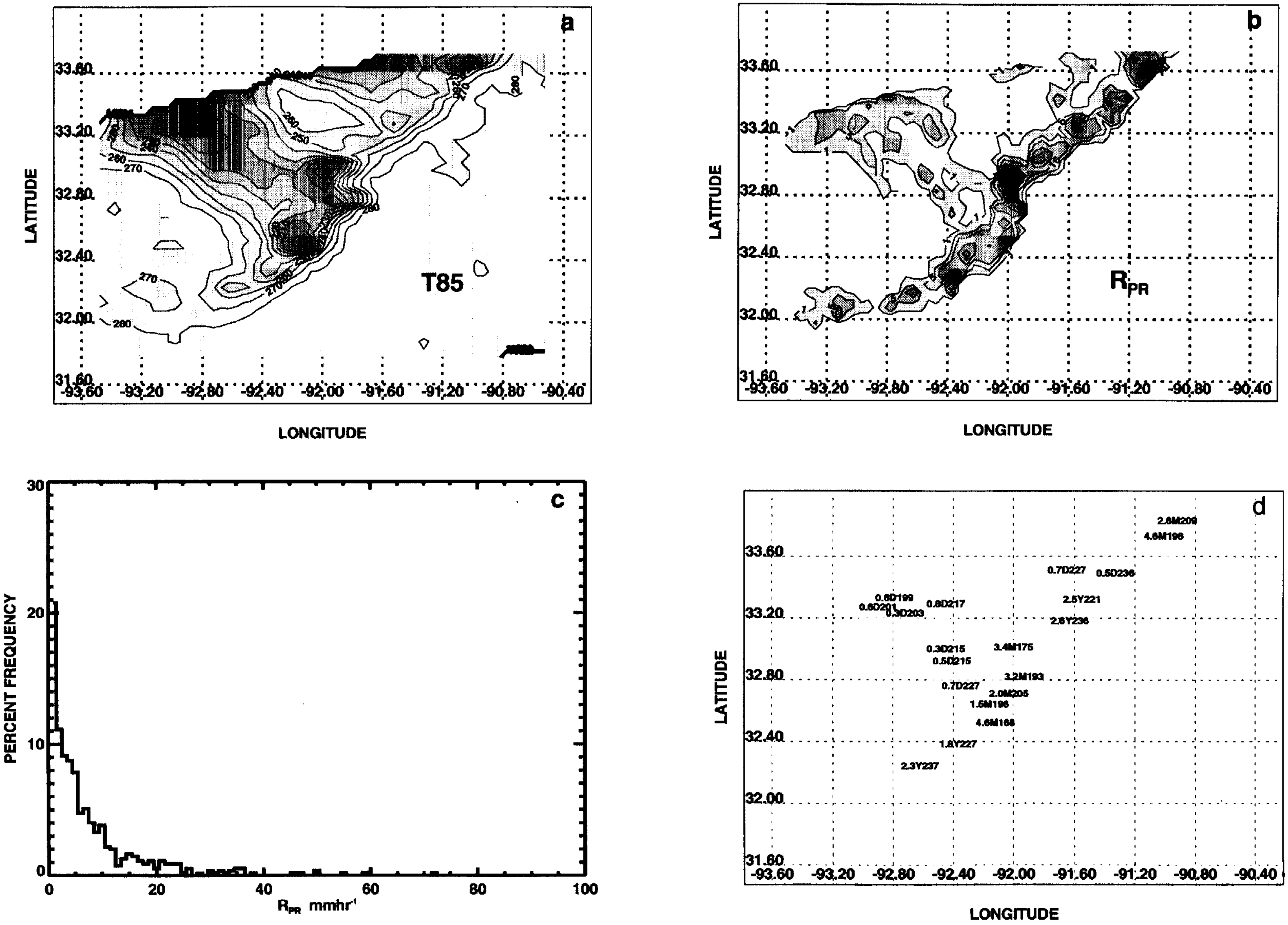

Figure 1: Data pertaining to a Mesoscale Convective System over the Southeast United States on June 5, 1998.

a) Map of 85 GHz brightness temperature, T85 (K), deduced from TMI.

b) Map of TRMM Precipitation Radar surface rain rate R_{PR} (mmhr-1).

c) Frequency distribution of surface rain rate for this event deduced from PR data.

d) Map of minima of T85 for this rain event indicating location of different types of thunderstorms - young (Y), mature (M) and decaying (D). The numbers shown on the left and right of the symbols Y, M and D indicate the magnitude of |dT85/dr| (Kkm^{-1}) and T85min (K).

rain map. These rain maxima represent the thunderstorms or Cbs. We may point out that a local minimum in T85 can be defined in the TMI data with respect to the brightness temperature values of its four neighboring footprints given by the TMI conical scans, as shown in Figure 2. Apparently, $T85_{min}$ can be produced in the radiometer footprints by dense ice particles that can strongly scatter microwave radiation in the narrow convective cells; or they can be produced by frozen and melting ice aggregates that can weakly scatter microwave radiation over a broader area. We note from Fig. 1a that we cannot identify the three different types of Cbs based simply on the magnitude of $T85_{min}$. In order to do such identification, we need to infer the spatial structure of the hydrometeors in the Cb. This structure can be assessed from the mean of the absolute values of the spatial gradients, i.e., $\overline{|dT85/dr|}$, within each Cb. Here, r represents the distance between a point in the Cb and the location of $T85_{min}$. This $\overline{|dT85/dr|}$ is determined utilizing the four neighboring footprint values as illustrated in Fig. 2, and it is analogous to the Laplacian ($\nabla^2 T85$) with an additional condition that T85 at the center point is a minimum.

Given the information $T85_{min}$ and $\overline{|dT85/dr|}$, we have developed, using PR rain rate as a guide, the following simple empirical model to identify young, mature, and decaying Cbs. First, because of narrow and relatively strong updrafts in the cloud cells of young and mature Cbs that contain dense ice hydrometeors, it is assumed that the mean gradient around $T85_{min}$, $\overline{|dT85/dr|}$, is large compared to that in the decaying Cbs. Thus, in this model we use a criterion based on $\overline{|dT85/dr|}$ to separate decaying Cbs from convectively active young and mature Cbs. Second, as a result of larger amounts of frozen rain drops and graupel, we expect mature Cbs to have magnitudes of $T85_{min}$ that are small in comparison to those found in young Cbs. Hence, the magnitude of a T85 minimum is used to separate the young and

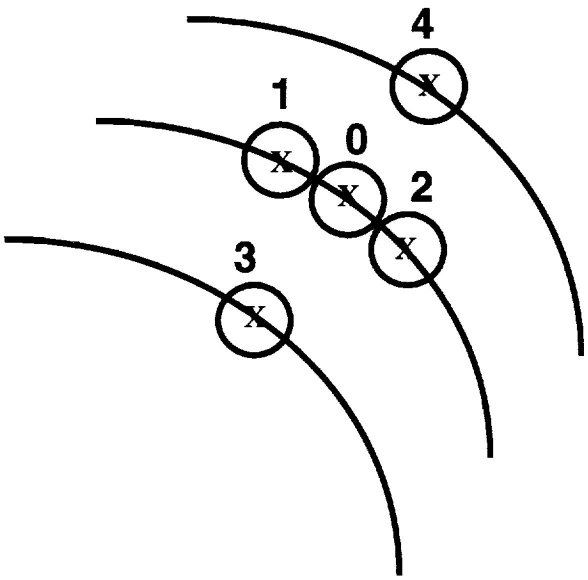

When $T_0 < T_1, T_2, T_3$ and T_4

Then $T_{min} = T_0$

$$\overline{\frac{dT}{dr}} \alpha \frac{A(T_1 + T_2) + B(T_3 + T_4) - 4T_0}{4}$$

Figure 2: Illustration of the method to determine the location of a T85 minimum, $T85_{min}$, and the mean spatial gradient, $\overline{|dT85/dr|}$, around this minimum. The solid curves represent the conical scan of the TMI radiometer, and the circles represent the footprints. Along the scan, the separation between footprints is about 4.6 km, while the separation between scans is about 13.9 km. In the illustration, the coefficients A and B correspond to appropriate weighting factors.

mature Cbs. The empirical scheme adopted here to separate the three types of Cbs is illustrated in Figure 3.

In Fig. 3, a scatterplot of $\overline{|dT85/dr|}$ versus $T85_{min}$ is shown. It is based on several Cbs from the sample of twelve dependent mesoscale rain events listed in Tables 2a and 3a. Six of these events are on land, and the other six are on ocean. As shown in this figure, we are assuming that the line $\overline{\mathbf{ab}}$ representing $\overline{|dT85/dr|}$ equal to 1 Kkm^{-1} separates the decaying Cbs from the young and mature convectively active Cbs. The decaying Cbs are assumed to have $\overline{|dT85/dr|}$ less than 1 Kkm^{-1}, while the active Cbs have $\overline{|dT85/dr|}$ greater than or equal to 1 Kkm^{-1}. The simple reason for this assumption is that we expect the ice hydrometeors will be relatively homogeneous in space in the decaying Cbs. On the other hand, the convectively active Cbs are not expected to have such homogeneity. From the figure, we may note that $T85_{min}$ is generally greater than 190 K for the decaying Cbs. This is not true of the convectively active Cbs. The young and mature Cbs are partitioned utilizing the threshold $T85_{min}$ equal to 210 K. This threshold is shown in Fig. 3 with the vertical line $\overline{\mathbf{ef}}$. However, we may point out that the 210 K value of this threshold is not critical. We find that within a reasonable range of the threshold (210 K > $T85_{min}$ > 190 K), our algorithm can be adjusted to get satisfactory rain retrievals. These criteria adopted to discriminate young, mature, and decaying Cbs are in broad agreement with radiative transfer models that consider dense ice particles and less dense ice aggregates.

In order to illustrate the correspondence between the Cbs indicated by the PR and the T85 data respectively shown in Figs. 1a and 1b, a map of the locations of $T85_{min}$ for the rain event of 5 June 1998 (Day 156) is shown in Figure 1d. The

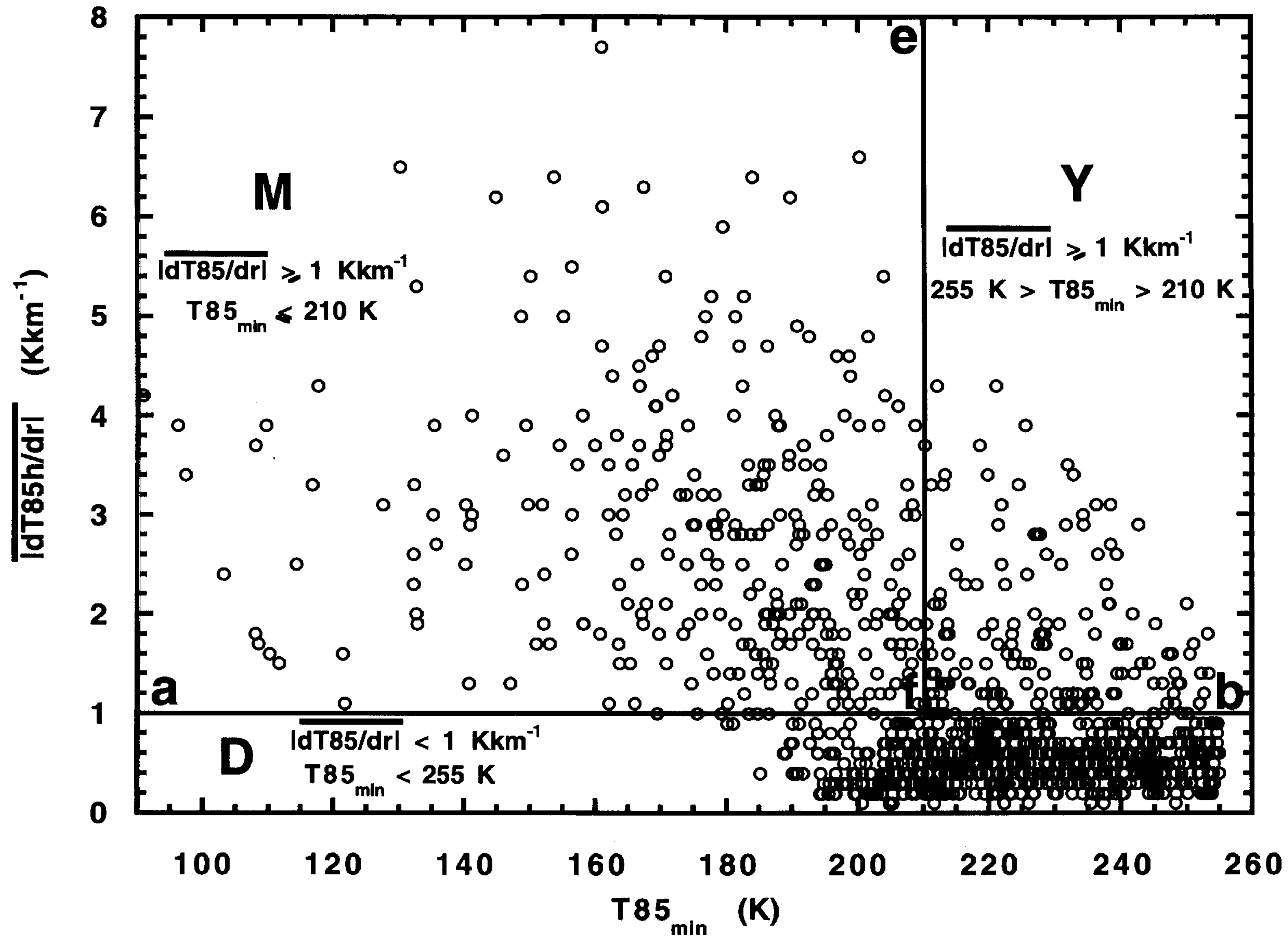

Figure 3: Scatterplot of $\overline{|dT85/dr|}$ versus T85$_{min}$ corresponding to decaying (D), young (Y), and mature (M) Cbs. The horizontal line $\overline{ab}$, where $\overline{|dT85/dr|}$ is equal to 1 Kkm^{-1}, separates the D Cbs from those of the Y and M categories. The vertical line $\overline{ef}$, where T85$_{min}$ is equal to 210 K, separates the Y from the M Cbs.

magnitudes of $T85_{min}$ and $\overline{|dT85/dr|}$, and the category of each Cb, are also shown in Fig. 1d.

We may note that, because factors such as evaporation below cloud, cloud liquid, and fractional cloud cover are highly variable, one cannot determine objectively a radiometer measured value of T85 which corresponds to a condition of zero rain at the surface. In our rain retrieval model, we assume that surface rain is zero in areas where T85 is greater than 260 K. Furthermore, all of the Cbs are assumed to have values of $T85_{min}$ less than 255 K. This is done to avoid weak Cbs that have $T85_{min}$ between 255 K and 260 K that lead to noise in the rain retrievals. Note also that in the present study the polarization in the 85 GHz, i.e., P85, is used to discriminate open ocean and wet surfaces on land from precipitating clouds where T85 is less than 260 K. A value of P85 greater than 15 K is used to screen out these surfaces. All rain rates discussed in this study (R_{TMI} - TMI Standard Rain Rate; R_{PR} - PR Standard Rain Rate; and **R** - Rain Rate derived from the present scheme) refer to rain rate near the surface.

In the present rain retrieval model, in order to blend the stratiform and convective rain rates in a smooth fashion, a weak background rain rate, R_S, is assumed to exist in all the areas where T85 is less than 260 K. This background rain is considered to be of stratiform type in the areas where Cbs are absent. For this purpose, the following linear relationship between the background rain rate, R_S, and T85 is used:

$$R_S = (260 - T85)\{dR_{PR}/dT85\}. \qquad (1)$$

Based on radar and radiometer observations, the sensitivity factor $dR_{PR}/dT85$ is set equal to 0.12.

As stated above, the rain rate in each Cb is superimposed on the background rain rate R_S. Each Cb is assumed to have a circular area with a radius of 10 km, with its center coinciding with the location of the pixel that has the minimum value $T85_{min}$. Note, one T85 pixel that defines a local minimum has an area of about 30 km^2. This local minimum leads us to infer the presence of a Cb extending over an area of about 310 km^2, which is about 10 pixels in our model. So the influence of a convective Cb is not limited to one pixel. Any pixel within the Cb is assigned an appropriate convective rain rate. Pixels outside of a given Cb are considered to have stratiform rain regardless of their T85 value. With the 5-pixel scheme utilized to identify local minima (see Fig. 2), we can find along a scan line two Cbs with one common pixel between them. Thus, there can be two Cbs along a radiometer scan line with a center-to-center separation distance of 9.2 km. In such a case, the two Cbs, each of which has a 10 km radius, will be overlapping. When there are such Cbs with different rain intensities overlapping with one another, we assume the rain rate in the overlapping area is governed by the more intense Cb. Thus, there can be several overlapping Cbs in a rain scene that can form large areas of convective rain.

We determine the Cb type as described earlier (see Fig. 3). Then based on the type, we estimate the mean rain rate in a Cb, excluding the background rain rate R_S, using one of the following three linear relationships:

Young Cbs
$$\overline{R}_Y = F_{10}\left[(255 - T85_{min})\{d\overline{R}_{PR}/dT85_{min}\}_Y\right]; \tag{2a}$$

Mature Cbs
$$\overline{R}_M = F_{10}\left[\overline{R}^*_Y + (210 - T85_{min})\{d\overline{R}_{PR}/dT85_{min}\}_M\right] \tag{2b}$$
$$\text{where } \overline{R}^*_Y = (255 - 210)\{d\overline{R}_{PR}/dT85_{min}\}_Y; \text{ and}$$

Decaying Cbs
$$\overline{R}_D = F_{10}\left[(255 - T85_{min})\{d\overline{R}_{PR}/dT85_{min}\}_D\right]. \tag{2c}$$

where $\overline{R}_Y$, $\overline{R}_M$, and $\overline{R}_D$ stand for mean rain rates of young, mature and decaying Cbs, respectively. This rain rate is superimposed on R_S to get total rain rate in each Cb. In Eqs. 2a and 2b, the sensitivity factors $(d\overline{R}_{PR}/dT85_{min})_Y$ and $(d\overline{R}_{PR}/dT85_{min})_M$ correspond to the convectively active young and mature Cbs, respectively. The term $\overline{R}_{PR}$ in these equations represents the radar derived mean rain rate over the circular area of the Cb, which has a radius of 10 km. As shown in Eq. 2c, another sensitivity factor $(d\overline{R}_{PR}/dT85_{min})_D$ is used for the decaying Cbs. These sensitivity factors are optimized with the help of the TMI and PR observations of a small sample of MCS cases. Over the ocean, the term F_{10} is set to vary linearly between 0.0 and 1.0 as the 10 GHz brightness temperature varies between 100 and 200 K, respectively. This can be expressed as

$$F10 = \begin{cases} 0.0 & T10 < 100K \\ (T10 - 100)/100 & 100K \le T10 \le 200K. \\ 1.0 & T10 > 200K \end{cases} \quad \textbf{(2d)}$$

The term F_{10} in Equation 2d is assigned a value of 1.0 over land regions, since T10 is greater than 200 K. In Table 1, we are presenting the magnitude of $d\overline{R}_{PR}/dT85_{min}$ for all Cb types.

As already indicated, the present rain retrieval model based on TMI data can estimate the mean rain rate in the Cbs on a scale of 20 km. In order to obtain the pattern of rain rate **R** everywhere in an MCS, including inside the Cbs, we use a simple interpolation procedure. As an example, we show below the interpolation equation applicable to young Cbs:

$$\mathbf{R} = R_S + \left[\overline{R}_Y - \{\overline{R}_Y/(T85_{Max} - \overline{T85})\}\ (T85 - \overline{T85})\right]. \quad (3)$$

Note that this interpolation scheme does not alter the average rain rate $\overline{R}_Y$ over the Cb area. Similar equations are applied to the mature and decaying Cbs. Here, T85 stands for the 85 GHz brightness temperature at any given point inside a Cb, and $T85_{Max}$ and $\overline{T85}$ stand for the maximum and mean values of T85 in that Cb. Outside a Cb, we set $\mathbf{R} = R_S$. Utilizing Eqs. 1, 2 and 3, in the present method we have derived the rain rate **R** everywhere in an MCS where T85 is less than 260 K.

We find the relationship of $\overline{R}_{PR}$ versus $T85_{min}$ for convective young and mature Cbs is significantly nonlinear over a wide 85 GHz brightness temperature range of about 255 K to 160 K. For simplicity, we fit this nonlinear relationship with two linear segments over this range. These two segments are separated at T85 equal to 210 K. We find for the decaying Cbs that the $\overline{R}_{PR}$ versus $T85_{min}$ relationship is weakly nonlinear, and so we represent it with one linear approximation over the entire temperature range. The sensitivity factors, i.e., $d\overline{R}_{PR}/dT85_{min}$ (see Table 1), given in Eqs. 2a, 2b, and 2c have to be optimized or tuned with the help of radar observations. This tuning procedure is discussed in the following section.

3. Tuning Procedure for the Rain Retrieval Model

For the purpose of optimization or tuning, we use a dependent sample of six rain events on land, and another sample of six rain events on ocean. For land, details pertaining to these events are listed in Tables 2a and 2b. For ocean, these details are listed in Tables 3a and 3b.

In the initial stage of the tuning procedure, preliminary estimates of the sensitivity factors needed in the retrieval algorithm are deduced as follows. For a given rain event, we identify the positions and the categories of Cbs with the help of $T85_{min}$ and $\overline{|dT85/dr|}$ (see for e.g. Fig. 1d). Then, for each Cb in that event, we can compute $\overline{R}_{PR}$ from the PR data. A similar procedure is applied to the remaining rain events, and a data set consisting of Cbs and their corresponding values of $\overline{R}_{PR}$ is developed. From this data set, we isolate one subset consisting of young Cbs. For that one subset, we determine a best linear fit between $T85_{min}$ and $\overline{R}_{PR}$. The slope of this linear fit for that Cb category gives us a preliminary estimate of the sensitivity factor $\{d\overline{R}_{PR}/dT85_{min}\}_Y$. In an analogous fashion, we determine preliminary values of the sensitivity factors $\{d\overline{R}_{PR}/dT85_{min}\}_M$ and $\{d\overline{R}_{PR}/dT85_{min}\}_D$ applicable to mature and decaying Cbs, respectively. The preliminary estimates of the sensitivity factors are then refined as follows.

Using Eqs. 1, 2a-2c, and 3, with the given sensitivity factors, we compute the spatial distribution of rain rates **R** for the 12 dependent mesoscale rain events[3] mentioned earlier. Then, utilizing the estimated values of **R** in the 2^ox3^o region that overlap with the PR scan area, the following seven quantities are calculated for each rain event:

- f^I, f^{II}, and f^{III} - quantities directly related to frequency of rain rate in three intervals, I) 1-10 $mmhr^{-1}$, II) 10-20 $mmhr^{-1}$, and III) greater than or equal to 20 $mmhr^{-1}$. These three quantities are simply the fractional rain areas corresponding to these three rain intervals.;
- $\langle \mathbf{R} \rangle_I$, $\langle \mathbf{R} \rangle_{II}$, and $\langle \mathbf{R} \rangle_{III}$ - mean rate rates in the three intervals;
- $\langle \mathbf{R} \rangle_A$ - area-average rain rate in the mesoscale region.

Note that these seven quantities are not independent of one another. They are inter-dependent.

---

[3] *These mesoscale rain events are represented using grid boxes of 2^0 lat. x 3^0 lon.. This choice of grid box size is compatible with the 220 km swath of the PR.*

To improve the preliminary values of the sensitivity factors, the ensemble means of each of the above seven quantities, denoted as $\overline{\langle\mathbf{R}\rangle}_{\mathrm{I}}$, $\overline{\langle\mathbf{R}\rangle}_{\mathrm{II}}$, $\overline{\langle\mathbf{R}\rangle}_{\mathrm{III}}$, $\bar{f}^{\mathrm{I}}$, $\bar{f}^{\mathrm{II}}$, $\bar{f}^{\mathrm{III}}$, and $\overline{\langle\mathbf{R}\rangle}_{\mathrm{A}}$, are computed from the dependent sample of six rain events separately for the land and ocean MCS cases. These ensemble means are compared with those given by the PR. Based on this comparison, adjustments are made to the sensitivity factors in Eqs. 2a, 2b, and 2c until these seven ensemble-mean quantities given by the radiometer and the corresponding quantities given by the radar converge to within about 15 % both on land and ocean.

We may note that the values of these sensitivity factors will depend on the criteria chosen for $T85_{\mathrm{min}}$ and $|dT85/dr|$, which are used to separate the three Cb categories (see Fig. 3). The above procedure gives us an optimized rain retrieval method that can be applied to a mesoscale region. In Tables 2a, 2b, 3a, and 3b, we show the results obtained from the six dependent MCS cases separately over land and ocean. However, since this sample of rain events is used in the tuning procedure, we have to demonstrate the applicability of this method with an independent set of rain events.

4. Application to Independent Cases

In order to show the general applicability of our algorithm, we have retrieved rain rates, $\mathbf{R}$, for 10 independent cases over land, and for the same number of cases over ocean. Also, over land and ocean, the TRMM Standard Rain Rates, R_{PR} and R_{TMI}, have been assembled for these cases. Here, the rain rates R_{PR} and R_{TMI} are the **Version 4** Official Standard Products of the TRMM Project. The relevant details pertaining to these events are listed in Tables 2a and 2b for land, and in Tables 3a and 3b for ocean.

The rain retrievals, R_{TMI} and $\mathbf{R}$, can be scrutinized with the mesoscale area-average rain rates, $\langle R_{TMI} \rangle_A$ and $\langle \mathbf{R} \rangle_A$. We find $\langle \mathbf{R} \rangle_A$ and $\langle R_{TMI} \rangle_A$ given in Tables 2b and 3b correlate well with those given by $\langle R_{PR} \rangle_A$. However, this result has limited significance. The correlation of mesoscale area-average rain rate does not guarantee quantitative agreement of the stratiform and convective rain distributions, and the associated latent heat release into the atmosphere (see for e.g., Simpson et al., 1996).

The merits of our retrieval algorithm can be assessed by comparing the frequency distribution of rain rate. This comparison is done in a gross fashion in this study as discussed in Section 3 by considering frequency of rain rate in three intervals: 1-10 mmhr^{-1} ($\bar{f}^{I}$), 10-20 mmhr^{-1} ($\bar{f}^{II}$) and greater than or equal to 20 mmhr^{-1} ($\bar{f}^{III}$). From Tables 2a and 3a, the frequency of rain rate in these three intervals deduced from $\mathbf{R}$ are shown to agree to within 15 % with those given by the PR both on land and ocean. On land, the TMI Standard Rain Rates, R_{TMI}, are not tuned to a radar. As a consequence, the frequency distribution given by R_{TMI} on land shows a poor agreement with PR. On ocean, the TMI Standard Rain Rates have been tuned to a radar. Thus, the lack of agreement in the frequency distribution of R_{TMI} over ocean reveals a weakness of the TMI Standard Rain Rates. This weakness has been pointed out in an independent assessment by Olson et al. (1999) (see Introduction).

In Tables 2b and 3b, we note $\overline{\langle \mathbf{R} \rangle}_{III}$ agrees to within 15 % of $\overline{\langle R_{PR} \rangle}_{III}$. Such a comparison of mean rain rates in the intervals I and II, not shown in the tables, also reveal an agreement to within 15 %. Similar statistics based on R_{TMI} show a poor agreement with those of the PR. From the independent sample of rain events, we contend that the algorithm developed here is capable of producing over land and ocean mean rain rates $\overline{\langle \mathbf{R} \rangle}_{I}$, $\overline{\langle \mathbf{R} \rangle}_{II}$, and $\overline{\langle \mathbf{R} \rangle}_{III}$, and their associated frequency distribution, that are in better agreement with that given by the radar.

In order to illustrate the properties of rain retrievals more vividly, we are presenting in Figures 4a-4c and 5a-5c maps of rain rate R_{PR}, R_{TMI}, and $\mathbf{R}$ for the following independent rain events on land: 1) an extensive MCS over Northern Argentina and Paraguay on 28 December 1998 (Day 362); and 2) an intense squall line with densely-packed convective cloud clusters over the Southern United States on 11 June 1998 (Day 162). As remarked earlier, since R_{TMI} is not tuned to radar on land, it does not reveal the convective features as seen in the maps of R_{PR}. On the other hand, the rain maps of $\mathbf{R}$ derived from our scheme show the convective features in better agreement with R_{PR}. In order to be comprehensive, we have deduced a detailed frequency distribution, or histogram, of rain rate from the maps of R_{PR}, R_{TMI}, and $\mathbf{R}$. We have also deduced for each rain event f^{I}, f^{II}, and f^{III}. Histograms, and numerical values of f^{I}, f^{II}, and f^{III} , for the two rain events on land are shown in Figures 4d-4f and 5d-5f.

We may point out that the rain map shown in Figure 5c, derived from our scheme, reveals reasonably well the intense rain from densely-packed convective cloud clusters observed along a squall line over the Southern United States on 11 June 1998 (Day 162). Some closely-spaced Cbs in Figure 5c form convective areas that have dimensions of about 40 km. The geographic distribution of intense rain given by our algorithm agrees well with that given by R_{PR}.

To illustrate the ability of our rain retrieval scheme over ocean, in Figures 6a-6c and 7a-7c we are presenting maps of rain rate R_{PR}, R_{TMI}, and $\mathbf{R}$ for two cases: 1)

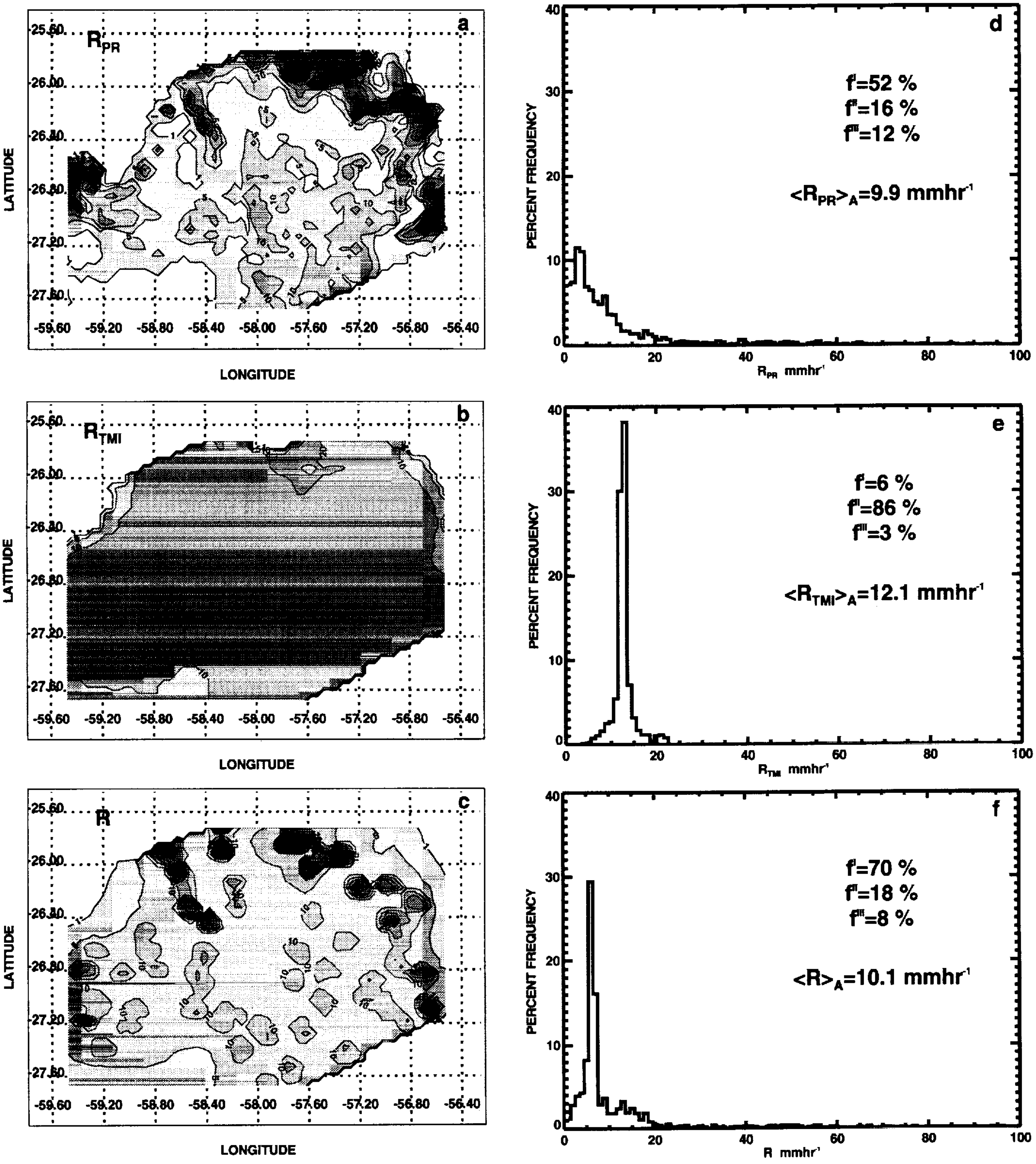

Figure 4: Maps of surface rain rate, and its frequency distribution, corresponding to a rain event that occurred over Northern Argentina and Paraguay on 28 December 1998 (Day 362).

a) map of PR rain rate, R_{PR} (mmhr-1).

b) map of TRMM Standard Rain Rate, R_{TMI} (mmhr-1), deduced from the microwave radiometer.

c) map of rain rate, **R** (mmhr-1), retrieved from our microwave radiometer algorithm.

d) frequeny distribution of PR rain rate, R_{PR} (mmhr-1).

e) frequeny distribution of TRMM Standard Rain Rate, R_{TMI}(mmhr-1), deduced from the microwave radiometer.

f) frequeny distribution of rain rate, **R** (mmhr-1), retrieved from our microwave radiometer algorithm.

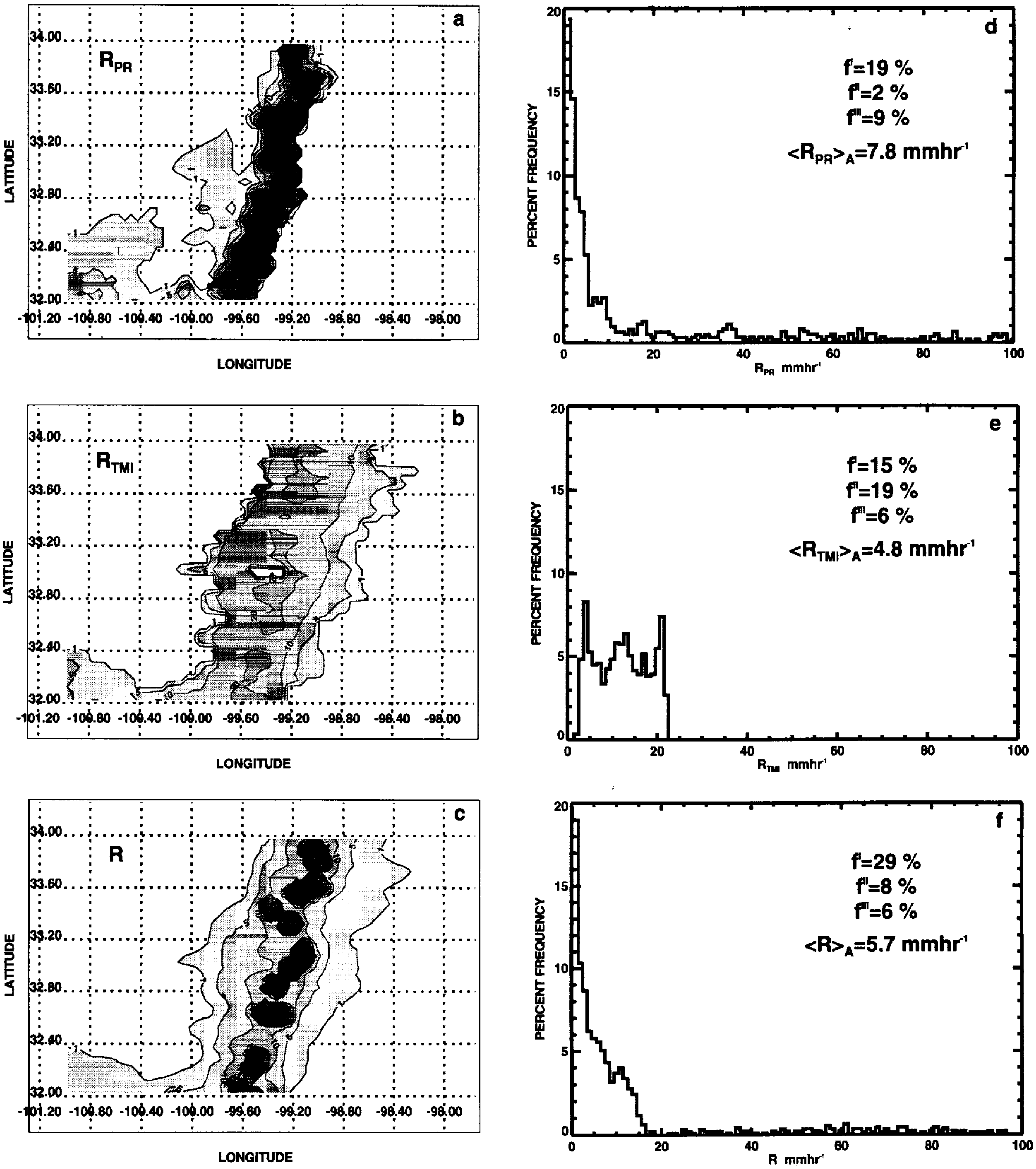

Figure 5: Maps of surface rain rate, and its frequency distribution, corresponding to a rain event that occurred over the Southern United States on June 11, 1998 (Day 162).

a) map of PR rain rate, R_{PR} (mmhr-1).

b) map of TRMM Standard Rain Rate, R_{TMI} (mmhr-1), deduced from the microwave radiometer.

c) map of rain rate, **R** (mmhr-1), retrieved from our microwave radiometer algorithm.

d) frequeny distribution of PR rain rate, R_{PR} (mmhr-1).

e) frequeny distribution of TRMM Standard Rain Rate, R_{TMI}(mmhr-1), deduced from the microwave radiometer.

f) frequeny distribution of rain rate, **R** (mmhr-1), retrieved from our microwave radiometer algorithm.

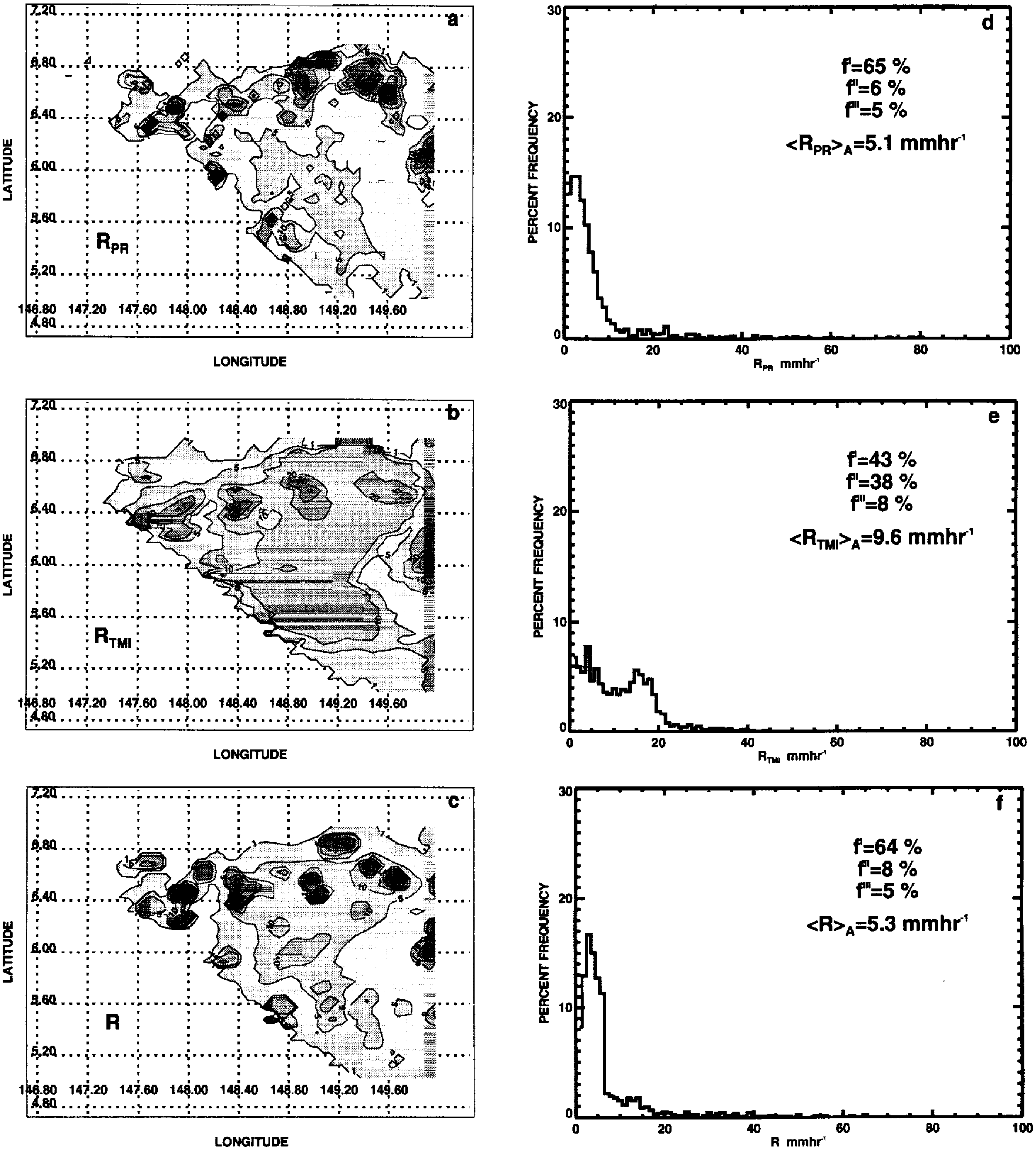

Figure 6: Maps of surface rain rate, and its frequency distribution, corresponding to a rain event that occurred over the Western Equatorial Pacific on January 24, 1999 (Day 24).

a) map of PR rain rate, R_{PR} (mmhr-1).

b) map of TRMM Standard Rain Rate, R_{TMI} (mmhr-1), deduced from the microwave radiometer.

c) map of rain rate, **R** (mmhr-1), retrieved from our microwave radiometer algorithm.

d) frequeny distribution of PR rain rate, R_{PR} (mmhr-1).

e) frequeny distribution of TRMM Standard Rain Rate, R_{TMI}(mmhr-1), deduced from the microwave radiometer.

f) frequeny distribution of rain rate, **R** (mmhr-1), retrieved from our microwave radiometer algorithm.

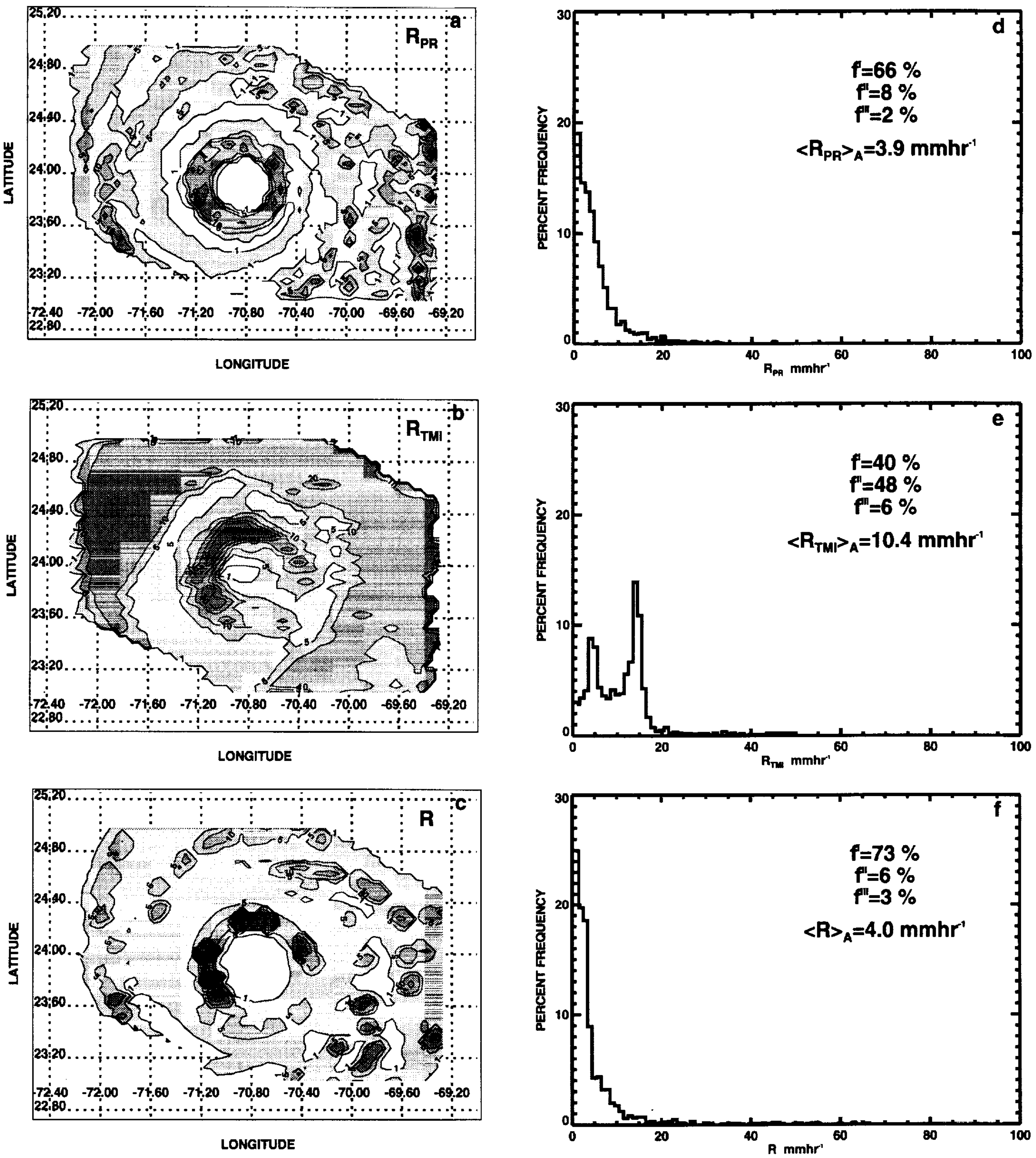

Figure 7: Maps of surface rain rate, and its frequency distribution, corresponding to Hurricane Floyd as it moved across the Western Atlantic on September 13, 1999 (Day 256).

a) map of PR rain rate, R_{PR} (mmhr-1).

b) map of TRMM Standard Rain Rate, R_{TMI} (mmhr-1), deduced from the microwave radiometer.

c) map of rain rate, **R** (mmhr-1), retrieved from our microwave radiometer algorithm.

d) frequeny distribution of PR rain rate, R_{PR} (mmhr-1).

e) frequeny distribution of TRMM Standard Rain Rate, R_{TMI}(mmhr-1), deduced from the microwave radiometer.

f) frequeny distribution of rain rate, **R** (mmhr-1), retrieved from our microwave radiometer algorithm.

the 24 January 1999 (Day 24) rain event over the Equatorial Western Pacific; and 2) Hurricane Floyd as it moved across the Western Atlantic Ocean on 13 September 1999 (Day 256). The Hurricane Floyd case is not one of the cases presented in Tables 3a and 3b. The histograms and numerical values f^{I}, f^{II} and f^{III} of rain rate given by R_{PR}, R_{TMI}, and $\mathbf{R}$ are shown in Figures 6d-6f and 7d-7f, respectively. From an examination of these figures we find the Standard Rain Rate R_{TMI}, when compared to R_{PR}, is not as good as $\mathbf{R}$ on the ocean.

The rain retrieval algorithm developed in this study is tuned to MCS cases over land and ocean. Such tuning does not guarantee its applicability to a hurricane event. The rain map of Hurricane Floyd shown in Fig. 7c, derived from our algorithm, captures in essence all the gross features found in the rain map of R_{PR} (Fig. 7a). For example, contrasts between large rain rates in the eyewall and spiral bands and light rain rates in the weak stratiform areas are captured better in our algorithm. Also, the histograms of R_{PR} (Fig. 7d) and $\mathbf{R}$ (Fig. 7f) have a log-normal character, while that given by R_{TMI} (Fig. 7e) does not.

In order to obtain a satisfactory convective and stratiform rain distribution from the measurements made by microwave radiometers, we find empirical tuning with collocated radar rain observations is needed. For this reason, the empirical rain retrieval scheme of Hong et al. (1999) has been tuned to a radar. This scheme is adopted to retrieve TMI Standard Rain Rates on ocean. However, Olson et al. (1999) point out the weakness of this algorithm in capturing quantitatively convective and stratiform rain over ocean. The reason for this weakness is that the scheme of Hong et al. (1999) does not have a way to limit convective rain area in an MCS to a thunderstorm scale. In the empirical rain retrieval algorithm developed in this study, convective rain in Cbs is limited to a thunderstorm scale. Hong et al. have not demonstrated the utility of their algorithm by tuning it with radar on land. Our rain retrieval scheme, developed with the help of the PR, can satisfactorily produce convective and stratiform rain rate distributions over both land and ocean.

The partitioning of convectively active thunderstorms, i.e., young and mature Cbs, from those that are decaying is critical for the determination of latent heat input into the atmosphere. In Figure 8, for all the MCS rain events over land and ocean, we show separately the frequency distributions of these active and decaying Cbs as a function of $T85_{min}$. From this figure, we see that the frequency distributions of the convectively active Cbs, both on land and ocean, tend to peak at a much colder $T85_{min}$ than the decaying Cbs. This vividly illustrates the stronger scattering effect of the dense ice particles in the active Cbs versus the less-dense ice aggregates in the decaying Cbs. This simple analysis presented in Fig. 8 lends support to the criterion $\overline{|dT85/dr|}$ used to classify the convectively active and decaying Cbs (see Fig. 3).

The present algorithm has the ability to retrieve rain in relatively warm clouds cells of young Cbs that have sufficient vertical growth to produce some ice. Purely warm rain where there is no ice formation will be missed in our algorithm. By comparing the PR rain with the rain retrieved from our algorithm, such missing warm rain can be identified. From such a comparison from several MCS events, we find missing warm rain area is less than about 5 % of the total rain area.

Based on the results and the comparison with the radar observations presented above, we note that the radiometer derived rain information can capture crudely the convective and stratiform rain character given by the PR. However, it is not capable of resolving fine details. The main advantage of our TMI rain retrieval

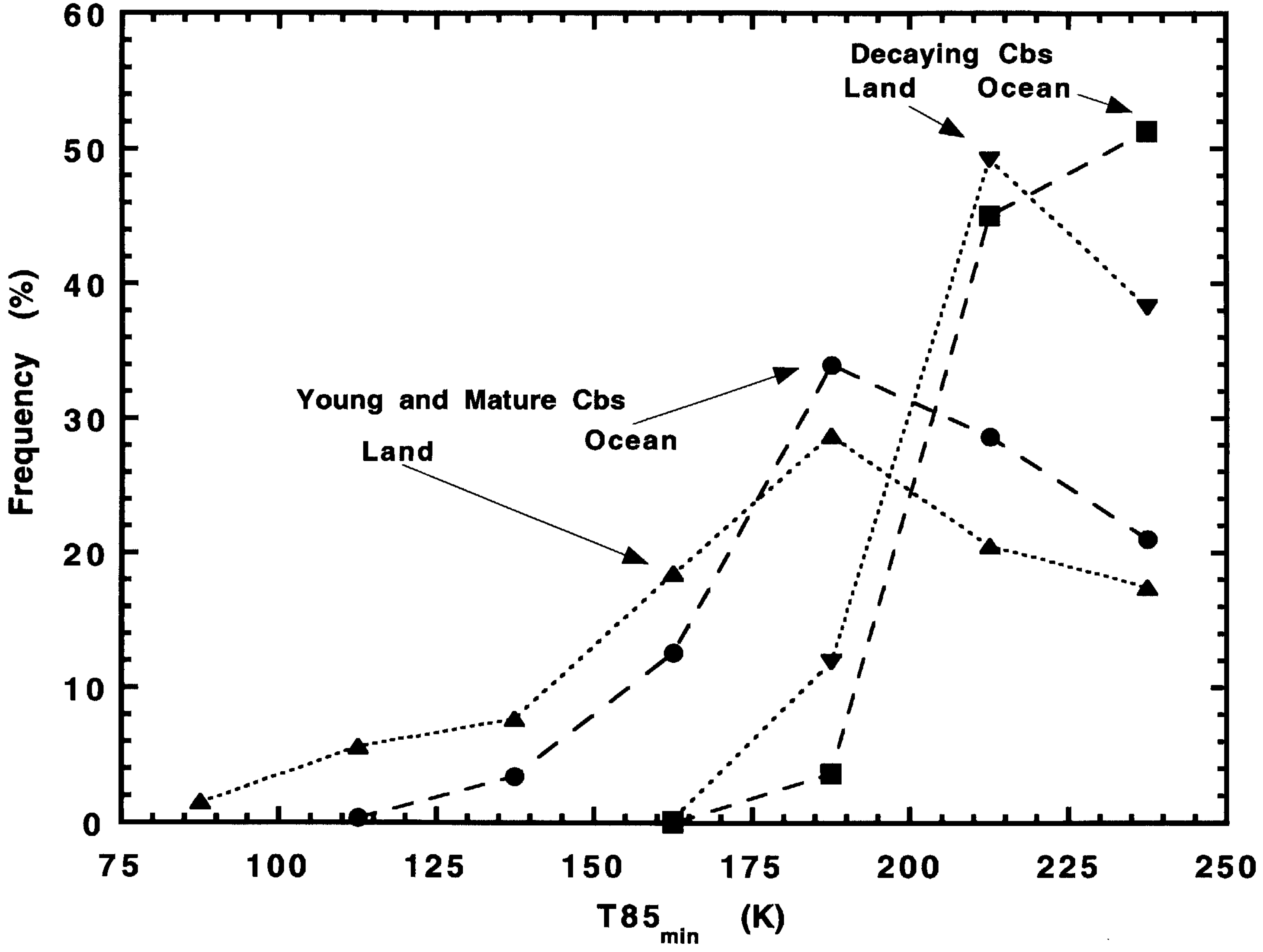

Figure 8: Frequency distribution of the convectively active young and mature thunderstorms, as well as the decaying thunderstorms, over land and ocean.

algorithm is that it can extend in a crude way the PR quality rain information to the 760 km swath width of the radiometer. As a result, one can obtain better estimates of latent heat release into the atmosphere over a wider area, which in turn can be used to improve general circulation models.

5. Conclusions

Multi-spectral, dual-polarization measurements made by satellite-borne microwave radiometers do not contain enough independent pieces of information to derive the amount and the vertical distribution of liquid, mixed phase, and frozen hydrometeors present in the atmosphere. This leads to uncertainties in quantitative estimation of rain rate pertaining to convective and stratiform rain based purely on radiative transfer theoretical considerations. Additional information, that is independent of the spectral measurements, is necessary to derive rain quantitatively. In Prabhakara et al. (1998, 1999), the fractional rain area in a mesoscale region derived from the microwave radiometer is used as additional information to derive mesoscale-average rain rate. The basis for this broad relationship is contained in the dynamics of Mesoscale Convective Systems which produce rain in that area. This method, based on fractional rain area, does not identify stratiform from convective rain areas.

In the last two decades, remote sensing of rain with the help of satellite-borne microwave radiometer observations has made significant progress. At present, the spatial resolution of the Tropical Rainfall Measuring Mission (TRMM) Microwave Imager (TMI) radiometer (~ 5.5 km at 85 GHz) has improved to the point that it can readily reveal some detailed information on a scale of thunderstorms, i.e., about 20 km. This capability is needed to retrieve convective rain. In the present method, we utilize TMI radiometer data, and the conceptual framework that thunderstorm scale dynamics (~ 20 km) establishes a relationship between the spatial distribution of T85 and the existence of Cbs of different types: *young, mature, and decaying.* A significant result of this study is that we can discriminate convectively active young and mature Cbs from stratiform or decaying Cbs. Also, we take into consideration radiative transfer properties (see for e.g. Schols et al., 1999) associated with the hydrometeors of these three different categories of Cbs, and infer relationships between the rain rate in these Cbs and $T85_{min}$. Initially, the rain rate observations made by the TRMM PR are used to tune these relationships. This entire procedure constitutes the basis for separation of convective rain from stratiform rain.

Results produced from independent rain events over land and ocean show a good consistency between our method and the PR. As a consequence of this capability, we can extend the rain information given by the 220 km swath of the PR to the full 760 km swath of the TMI. The method developed here is computationally simple and fast, and can be used as an effective tool to generate the climatology of precipitation over tropical land and ocean.

We may bring to the attention of the reader some assumptions and weaknesses in the present rain retrieval method. We are assuming that all Cbs, regardless of their type, have a circular shape. The strong updrafts in the Cbs may be tilted, which leads to a given T85 minimum that does not collocate with the actual center of the Cb. This mislocation is ignored. The actively developing and decaying portions of a Cb that may be close together (Houze, 1997) are not resolved in the present method. At the wavelength used by the PR (~ 2 cm), attenuation at high rain rates can be significant. When the rain rate is high, this can introduce errors in the PR rain rate estimates. Since our algorithm is tuned to the PR data, errors in the PR rain estimates will be reflected in our retrievals.

The empirical rain retrieval method developed here, with the aid of the PR, can serve as a useful tool for retrieving rain over the 760 km swath of the TMI. However, this radiometer derived rain information can capture only the gross character of the radar observations, and not the fine details. Improvement in the spatial resolution of the microwave radiometer, and better methods to identify different kinds of hydrometeors, will be helpful in advancing the remote sensing capability.

References

Adler, R. F. and A. J. Negri, 1988: A satellite infrared technique to estimate tropical convection and stratiform rainfall. *J. Appl. Met.* , **27**, 30-51.

Battan, L. J., 1973: *Radar Observations of the Atmosphere*. The University of Chicago Press, 324 pp.

Conner, M. D., and G. W. Petty, 1998: Validation and intercomparison of SSM/I rain-rate retrieval methods over the continental United States. *J. Appl. Met.*, **37**, 679-700.

Doneaud, A. A., S. Ionescu-Niscov, D. L. Priegnitz, and P. L. Smith, 1984: The Area Time Integral as an indicator for convective rain volume. *J. Clim. Appl. Met*, **23** , 555-561.

Ebert, E. E., M. J. Manton, P. A. Arkin, R. J. Allam, G. E. Holpin, and A. Gruber, 1996: Results from the GPCP Algorithm Intercomparison Programme. *Bull. of Am. Met Soc.*, **77**, 2875-2887.

Heymsfield, G. M., I. J. Caylor, J. M. Shepherd, W. S. Olson, S. W. Bidwell, W. C. Boncyk, and S. Ameen. 1996: Structure of Florida thunderstorms using high altitude aircraft radiometer and radar observations. *J. Appl. Met*, **35**, 1736-1762.

Hollinger, J., R. C. Lo, G. Poe, R. Savage, and J. Pierce, 1987: *Special Sensor Microwave Imager Guide*. Naval Research Laboratory, Washington, D.C., 120 pp.

Hong, Y., C. D. Kummerow, and W. S. Olson, 1999: Separation of convective and stratiform precipitation using microwave brightness temperature. *J. Appl. Met.* , **38**, 1193-1213.

Houze Jr., R. A. and A. K. Betts, 1981: Convection in GATE. *Rev. Geophys. and Space Phys.*, **41**, 541-576.

Houze Jr., R. A., 1993: Cloud Dynamics. Academic Press, Inc., San Diego, 571 pp.

Houze Jr., R. A., 1997: Stratiform precipitation in regions of convection: A meteorological paradox? *Bull. Amer. Met. Soc.*, **78**, 2179-2196.

Jones, D. M. A. and A. L. Sims, 1978: Climatology of instantaneous rainfall rates. *J. Appl. Met.*, **17**, pp. 1135-1140.

Kummerow, C., R. A. Mack, and I. M. Hakkarinen, 1989: A self-consistency approach to improved microwave rainfall estimation from space. *J. Appl. Met*, **28**, 869-884.

Kummerow, C., 1998: Beamfilling errors in passive microwave rainfall retrievals. *J. Appl. Met.* , **37**, 356-370.

Lopez, R. E., D. Atlas, D. Rosenfeld, J. L. Thomas, D. O. Blanchard, and R. L. Holle, 1989: Estimation of rainfall using the Radar Echo Area Time Integral. *J. Appl. Met*, **28**, 1162-1175.

McGhaughey, G. and E. Zipser, 1996: Passive microwave observations of the stratiform regions of two tropical oceanic Mesoscale Convective Systems. *J. Appl. Met*, **35**, 1949-1962.

Oki, R., A. Sumi, D. A. Short, 1997: Sampling simulation of TRMM rainfall estimation using Radar-AMeDAS composites. *J. Appl. Met*, **36**, 1480-1492.

Olson, W. S., C. Kummerow, G. M. Heymsfield, and L. Giglio, 1996: A method for combined passive-active microwave retrievals of cloud and precipitation profiles. *J. Appl. Met*, **35**, 1763-1789.

Olson, W. S., C. Kummerow, Y. Hong, and W.-K. Tao, 1999: Atmospheric latent heating distributions in the tropics derived from satellite passive microwave radiometer measurements. *J. Appl. Met*, **38**, 633-664.

Prabhakara, C., G. Dalu, G. L. Liberti, J. J. Nucciarone, and R. Suhasini, 1992: Rainfall over oceans : Remote sensing from satellite microwave radiometers. *Met and Atmos. Phys.*, **47**, 177-199.

Prabhakara C., J. J. Nucciarone, and J.-M. Yoo, 1995: Examination of Global Atmospheric Temperature Monitoring with Satellite Microwave Measurements 1) Theoretical Consideration. *Climatic Change*, **30**, 349-366.

Prabhakara, C., R. Iacovazzi, Jr., R. Meneghini, R. Oki, D. A. Short, M. Cadeddu, and J. A. Weinman, 1998: A TRMM microwave radiometer rain retrieval technique based on fractional rain area, *J. Met. Soc. Japan* , **76**, 765-781.

Prabhakara, C., R. Iacovazzi, Jr., R. Oki, J. A. Weinman, 1999: A microwave radiometer rain retrieval method applicable to land areas, *J. Met. Soc. Japan* , **77**, 859-871.

Schols, J. L., J. A. Weinman, R. E. Stewart, and R. P. Lawson, 1995: The retrieval of dry and wet snow distributions from SSM/I measurements and MM5 forecast results. *Proceedings of International Geosciences and Remote Sensing Symposium*. IGARSS'95.

Schols, J. L., J. A. Weinman, G.D. Alexander, R. E. Stewart, L.J. Angus, and A.C.L. Lee, 1999: Microwave properties of frozen precipitation around a North Atlantic cyclone. *J. Appl. Met.*, **38**, 29-43.

Simpson, J., C. Kummerow, W.-K. Tao, and R. F. Adler, 1996: On the tropical rainfall measuring mission (TRMM). *Met and Atmos. Phys.*, **60**, 19-36.

Smith, E. A. and A. Mugnai, 1992: Foundations for statistical-physical precipitation retrieval from passive microwave satellite measurements. Part 1: Brightness temperature properties of a time-dependent cloud radiation model. *J. Appl. Met*, **31**, 532-552.

Steiner, M., R. A. Houze, and S. E. Yuter, 1995: Climatological characterization of three-dimensional storm structure from operational radar and rain gauge data, *J. Appl. Met.* , **34**, 1978-2007.

Tokay, A., and D. A. Short, 1996: Evidence from tropical raindrop spectra of the origin of rain from stratiform versus convective clouds. *J. Appl. Meteor.*, **35**, 355-371.

Wu, R. and J. A. Weinman, 1984: Microwave radiances from precipitating clouds containing aspherical ice, combined phase, and liquid hydrometeors. *J. Geophy. Res.*, **89**, 7170-7178.

Figure Captions

Figure 1: Data pertaining to a Mesoscale Convective System over the Southeast United States on June 5, 1998 (Day 156).

a) Map of 85 GHz brightness temperature, T85 (K), deduced from TMI.

b) Map of TRMM Precipitation Radar surface rain rate R_{PR} (mmhr^{-1}).

c) Frequency distribution of surface rain rate for this event deduced from PR data.

d) Map of minima of T85 for this rain event indicating location of different types of thunderstorms - young (Y), mature (M) and decaying (D). The numbers shown on the left and right of the symbols Y, M and D indicate the magnitude of $\overline{|dT85/dr|}$ (Kkm^{-1}) and $T85_{min}$ (K).

Figure 2: Illustration of the method to determine the location of a T85 minimum, $T85_{min}$, and the mean spatial gradient, $\overline{|dT85/dr|}$, around this minimum. The solid curves represent the conical scan of the TMI radiometer, and the circles represent the footprints. Along the scan, the separation between footprints is about 4.6 km, while the separation between scans is about 13.9 km. In the illustration, the coefficients A and B correspond to appropriate weighting factors.

Figure 3: Scatterplot of $\overline{|dT85/dr|}$ versus $T85_{min}$ corresponding to decaying (D), young (Y), and mature (M) Cbs. The horizontal line $\overline{\mathbf{ab}}$, where $\overline{|dT85/dr|}$ is equal to 1 Kkm^{-1}, separates the D Cbs from those of the Y and M categories. The vertical line $\overline{\mathbf{ef}}$, where $T85_{min}$ is equal to 210 K, separates the Y from the M Cbs.

Figure Captions Continued

Figure 4: Maps of surface rain rate, and its frequency distribution, corresponding to a rain event that occurred over Northern Argentina and Paraguay on 28 December 1998 (Day 362).

a) map of PR rain rate, R_{PR} (mmhr^{-1}).

b) map of TRMM Standard Rain Rate, R_{TMI} (mmhr^{-1}), deduced from the microwave radiometer.

c) map of rain rate, **R** (mmhr^{-1}), retrieved from our microwave radiometer algorithm.

d) frequency distribution of PR rain rate, R_{PR} (mmhr^{-1}).

e) frequency distribution of TRMM Standard Rain Rate, R_{TMI} (mmhr^{-1}), deduced from the microwave radiometer.

f) frequency distribution of rain rate, **R** (mmhr^{-1}), retrieved from our microwave radiometer algorithm.

Figure Captions Continued

Figure 5: Maps of surface rain rate, and its frequency distribution, corresponding to a rain event that occurred over the Southern United States on June 11, 1998 (Day 162).

a) map of PR rain rate, R_{PR} (mmhr^{-1}).

b) map of TRMM Standard Rain Rate, R_{TMI} (mmhr^{-1}), deduced from the microwave radiometer.

c) map of rain rate, $\mathbf{R}$ (mmhr^{-1}), retrieved from our microwave radiometer algorithm.

d) frequency distribution of PR rain rate, R_{PR} (mmhr^{-1}).

e) frequency distribution of TRMM Standard Rain Rate, R_{TMI} (mmhr^{-1}), deduced from the microwave radiometer.

f) frequency distribution of rain rate, $\mathbf{R}$ (mmhr^{-1}), retrieved from our microwave radiometer algorithm.

Figure Captions Continued

Figure 6: Maps of surface rain rate, and its frequency distribution, corresponding to a rain event that occurred over the Western Equatorial Pacific on January 24, 1999 (Day 24).

a) map of PR rain rate, R_{PR} (mmhr^{-1}).

b) map of TRMM Standard Rain Rate, R_{TMI} (mmhr^{-1}), deduced from the microwave radiometer.

c) map of rain rate, **R** (mmhr^{-1}), retrieved from our microwave radiometer algorithm.

d) frequency distribution of PR rain rate, R_{PR} (mmhr^{-1}).

e) frequency distribution of TRMM Standard Rain Rate, R_{TMI} (mmhr^{-1}), deduced from the microwave radiometer.

f) frequency distribution of rain rate, **R** (mmhr^{-1}), retrieved from our microwave radiometer algorithm.

Figure Captions Continued

Figure 7: Maps of surface rain rate, and its frequency distribution, corresponding to Hurricane Floyd as it moved across the Western Atlantic Ocean on September 13, 1999 (Day 256).

a) map of PR rain rate, R_{PR} (mmhr^{-1}).

b) map of TRMM Standard Rain Rate, R_{TMI} (mmhr^{-1}), deduced from the microwave radiometer.

c) map of rain rate, $\mathbf{R}$ (mmhr^{-1}), retrieved from our microwave radiometer algorithm.

d) frequency distribution of PR rain rate, R_{PR} (mmhr^{-1}).

e) frequency distribution of TRMM Standard Rain Rate, R_{TMI} (mmhr^{-1}), deduced from the microwave radiometer.

f) frequency distribution of rain rate, $\mathbf{R}$ (mmhr^{-1}), retrieved from our microwave radiometer algorithm.

Figure 8: Frequency distribution of the convectively active young and mature thunderstorms, as well as the decaying thunderstorms, over land and ocean.

Table 1: Sensitivity of $T85_{min}$ to the Cb mean surface rain rate $\overline{R}_{PR}$ applicable to tropical land and ocean regions.

Cb Type	**85 GHz Minimum**	**Sensitivity Factors** $d\overline{R}_{PR}/dT85_{min}$
Young	$255\ K > T85_{min} > 210\ K$	$0.25\ mmhr^{-1}K^{-1}$
Mature	$T85_{min} < 210\ K$	$0.35\ mmhr^{-1}K^{-1}$
Decaying	$255\ K > T85_{min}$	$0.12\ mmhr^{-1}K^{-1}$

Table 2a: ***Land*** dependent and independent MCS events and the associated fractional rain area statistics. The fractional rain area is calculated for each of the following rain rate intervals: I) 1-10 mmhr^{-1}, II) 10-20 mmhr^{-1}, and III) greater than or equal to 20 mmhr^{-1}.

Dependent Cases

Day/Yr	Lat	Lon	f^{I}	f^{I}_{PR}	f^{I}_{TMI}	f^{II}	f^{II}_{PR}	f^{II}_{TMI}	f^{III}	f^{III}_{PR}	f^{III}_{TMI}
156/98	32.8	-92.0	0.21	0.19	0.09	0.03	0.04	0.12	0.02	0.02	0.0
159/98	12.5	-1.4	0.34	0.17	0.03	0.04	0.02	0.24	0.03	0.02	0.0
169/98	26.9	115.7	0.57	0.51	0.35	0.04	0.03	0.25	0.02	0.01	0.0
171/98	25.8	115.0	0.22	0.19	0.17	0.01	0.02	0.02	0.02	0.01	0.0
180/98	32.8	160.0	0.27	0.28	0.11	0.04	0.06	0.21	0.02	0.04	0.0
201/98	28.9	116.0	0.29	0.25	0.07	0.02	0.02	0.18	0.03	0.01	0.0
MEAN			**0.32**	**0.27**	**0.14**	**0.03**	**0.03**	**0.17**	**0.02**	**0.02**	**0.00**

Independent Cases

Day/Yr	Lat	Lon	f^{I}	f^{I}_{PR}	f^{I}_{TMI}	f^{II}	f^{II}_{PR}	f^{II}_{TMI}	f^{III}	f^{III}_{PR}	f^{III}_{TMI}
146/98	35.0	-89.5	0.48	0.38	0.17	0.06	0.11	0.37	0.04	0.08	0.0
156/98	35.0	-89.1	0.62	0.47	0.12	0.10	0.13	0.56	0.06	0.09	0.02
160/98	4.4	-66.2	0.45	0.47	0.39	0.02	0.02	0.05	0.0	0.0	0.0
162/98	33.0	-99.5	0.29	0.19	0.15	0.08	0.02	0.19	0.06	0.09	0.06
162/98	31.7	115.6	0.36	0.31	0.25	0.02	0.01	0.04	0.0	0.0	0.0
186/98	24.0	81.5	0.44	0.49	0.18	0.06	0.06	0.31	0.03	0.03	0.0
271/98	31.5	-87.0	0.76	0.72	0.48	0.06	0.10	0.35	0.02	0.03	0.00
362/98	-26.7	-58.0	0.70	0.52	0.06	0.18	0.16	0.86	0.08	0.12	0.03
19/99	-17.9	29.8	0.32	0.40	0.19	0.04	0.03	0.12	0.03	0.02	0.0
44/99	-17.2	127.5	0.43	0.28	0.15	0.05	0.05	0.31	0.06	0.04	0.01
MEAN			**0.48**	**0.42**	**0.21**	**0.07**	**0.07**	**0.32**	**0.04**	**0.05**	**0.01**

Table 2b: *Land* dependent and independent MCS events and the associated mesoscale-mean rain statistics. The mean rain rate is calculated for each of the following rain rate intervals: I) 1-10 mmhr^{-1}, II) 10-20 mmhr^{-1}, and III) greater than or equal to 20 mmhr^{-1}.

Dependent Cases

Day/Yr	Lat	Lon	$\langle R\rangle_{III}$	$\langle R_{PR}\rangle_{III}$	$\langle R_{TMI}\rangle_{III}$	$\langle R\rangle_{A}$	$\langle R_{PR}\rangle_{A}$	$\langle R_{TMI}\rangle_{A}$
156/98	32.8	-92.0	31.3	32.0	0.0	1.7	1.9	2.0
159/98	12.5	-1.4	37.3	30.5	20.0	3.2	1.4	3.2
169/98	26.9	115.7	33.4	30.0	0.0	2.9	2.3	5.1
171/98	25.8	115.0	35.7	34.9	0.0	1.3	1.1	1.2
180/98	32.8	160.0	30.3	30.5	0.0	2.1	3.1	3.0
201/98	28.9	116.0	32.8	25.1	0.0	2.1	1.1	2.6
MEAN			**33.5**	**30.5**	**3.3**	**2.2**	**1.8**	**2.9**

Independent Cases

Day/Yr	Lat	Lon	$\langle R\rangle_{III}$	$\langle R_{PR}\rangle_{III}$	$\langle R_{TMI}\rangle_{III}$	$\langle R\rangle_{A}$	$\langle R_{PR}\rangle_{A}$	$\langle R_{TMI}\rangle_{A}$
146/98	35.0	-89.5	39.4	38.2	0.0	4.4	6.3	5.6
156/98	35.0	-89.1	40.2	44.2	25.5	6.8	7.7	8.4
160/98	4.4	-66.2	26.0	32.3	0.0	1.5	1.7	2.8
162/98	33.0	-99.5	61.6	75.1	20.8	5.7	7.8	4.8
162/98	31.7	115.6	24.8	21.5	0.0	1.2	.7	2.0
186/98	24.0	81.5	33.3	28.4	0.0	3.4	3.4	4.8
271/98	31.5	-87.0	29.3	27.0	0.0	3.6	5.1	7.1
362/98	-26.7	-58.0	42.1	45.2	20.9	10.1	9.9	12.1
19/99	-17.9	29.8	36.8	28.8	20.0	2.4	2.0	2.6
44/99	-17.2	127.5	42.3	32.8	20.5	5.0	3.0	5.2
MEAN			**37.6**	**37.4**	**10.8**	**4.4**	**4.8**	**5.5**

Table 3a: *Ocean* dependent and independent MCS events and the associated fractional rain area statistics. The fractional rain area is calculated for each of the following rain rate intervals: I) 1-10 mmhr^{-1}, II) 10-20 mmhr^{-1}, and III) greater than or equal to 20 mmhr^{-1}.

Dependent Cases

Day/Yr	Lat	Lon	f^{I}	f^{I}_{PR}	f^{I}_{TMI}	f^{II}	f^{II}_{PR}	f^{II}_{TMI}	f^{III}	f^{III}_{PR}	f^{III}_{TMI}
159/98	-9.5	85.0	0.33	0.44	0.46	0.02	0.02	0.17	0.01	0.00	0.01
162/98	13.6	-105.2	0.41	0.39	0.51	0.02	0.02	0.06	0.01	0.01	0.03
184/98	3.9	-91.8	0.47	0.45	0.56	0.04	0.06	0.15	0.03	0.03	0.05
314/98	5.5	147.2	0.63	0.61	0.62	0.06	0.08	0.35	0.04	0.03	0.06
7/99	4.5	156.0	0.45	0.46	0.55	0.04	0.03	0.14	0.01	0.01	0.03
70/99	-25.2	54.0	0.59	0.58	0.54	0.02	0.02	0.20	0.0	0.00	0.01
MEAN			**0.48**	**0.49**	**0.54**	**0.03**	**0.04**	**0.18**	**0.02**	**0.01**	**0.03**

Independent Cases

Day/Yr	Lat	Lon	f^{I}	f^{I}_{PR}	f^{I}_{TMI}	f^{II}	f^{II}_{PR}	f^{II}_{TMI}	f^{III}	f^{III}_{PR}	f^{III}_{TMI}
154/98	6.3	-13.0	0.59	0.47	0.64	0.02	0.04	0.25	0.01	0.02	0.01
158/98	21.0	118.2	0.38	0.28	0.48	0.01	0.01	0.04	0.01	0.02	0.02
244/98	26.1	-90.6	0.45	0.40	0.59	0.04	0.06	0.14	0.02	0.02	0.04
269/98	8.5	-129.8	0.41	0.36	0.46	0.03	0.03	0.13	0.0	0.0	0.01
335/98	1.0	147.0	0.31	0.24	0.34	0.01	0.01	0.03	0.01	0.01	0.01
24/99	6.0	148.5	0.64	0.65	0.43	0.08	0.06	0.38	0.05	0.05	0.08
63/99	-0.4	-36.0	0.55	0.36	0.45	0.05	0.06	0.14	0.02	0.02	0.03
65/99	-14.4	102.4	0.71	0.64	0.62	0.06	0.05	0.12	0.04	0.06	0.12
68/99	-27.0	-29.6	0.38	0.27	0.47	0.06	0.05	0.13	0.03	0.04	0.06
73/99	-25.9	168.8	0.59	0.47	0.54	0.01	0.01	0.06	0.01	0.01	0.02
MEAN			**0.50**	**0.41**	**0.50**	**0.04**	**0.04**	**0.14**	**0.02**	**0.02**	**0.04**

Table 3b: *Ocean* dependent and independent MCS events and the associated mesoscale-mean rain statistics. The mean rain rate is calculated for each of the following rain rate intervals: I) 1-10 mmhr^{-1}, II) 10-20 mmhr^{-1}, and III) greater than or equal to 20 mmhr^{-1}.

Dependent Cases

Day/Yr	Lat	Lon	$\langle R \rangle_{III}$	$\langle R_{PR} \rangle_{III}$	$\langle R_{TMI} \rangle_{III}$	$\langle R \rangle_{A}$	$\langle R_{PR} \rangle_{A}$	$\langle R_{TMI} \rangle_{A}$
159/98	-9.5	85.0	21.8	20.0	24.5	1.5	1.6	4.2
162/98	13.6	-105.2	30.2	28.5	26.9	1.9	1.5	3.3
184/98	3.9	-91.8	34.4	29.5	31.1	3.3	3.2	6.0
314/98	5.5	147.2	30.5	28.6	25.1	4.2	4.4	8.3
7/99	4.5	156.0	28.2	32.4	22.7	2.3	2.4	4.5
70/99	-25.2	54.0	20.3	21.2	24.6	2.3	1.9	4.9
MEAN			**27.6**	**26.7**	**25.8**	**2.6**	**2.5**	**5.2**

Independent Cases

Day/Yr	Lat	Lon	$\langle R \rangle_{III}$	$\langle R_{PR} \rangle_{III}$	$\langle R_{TMI} \rangle_{III}$	$\langle R \rangle_{A}$	$\langle R_{PR} \rangle_{A}$	$\langle R_{TMI} \rangle_{A}$
154/98	6.3	-13.0	29.3	29.4	25.3	2.0	2.5	5.7
158/98	21.0	118.2	32.5	37.9	25.8	1.5	1.6	2.2
244/98	26.1	-90.6	30.8	30.4	27.3	2.6	2.8	5.1
269/98	8.5	-129.8	22.3	22.9	21.8	1.7	1.6	3.6
335/98	1.0	147.0	28.8	37.4	23.9	1.2	1.0	1.7
24/99	6.0	148.5	33.0	33.0	25.4	5.3	5.1	9.6
63/99	-0.4	-36.0	30.3	25.2	26.2	3.4	2.7	4.7
65/99	-14.4	102.4	40.6	44.2	40.1	4.9	4.9	8.7
68/99	-27.0	-29.6	29.4	35.0	24.9	3.2	3.0	5.0
73/99	-25.9	168.8	37.5	28.3	28.8	1.9	1.6	2.6
MEAN			**31.4**	**32.4**	**27.0**	**2.8**	**2.7**	**4.9**

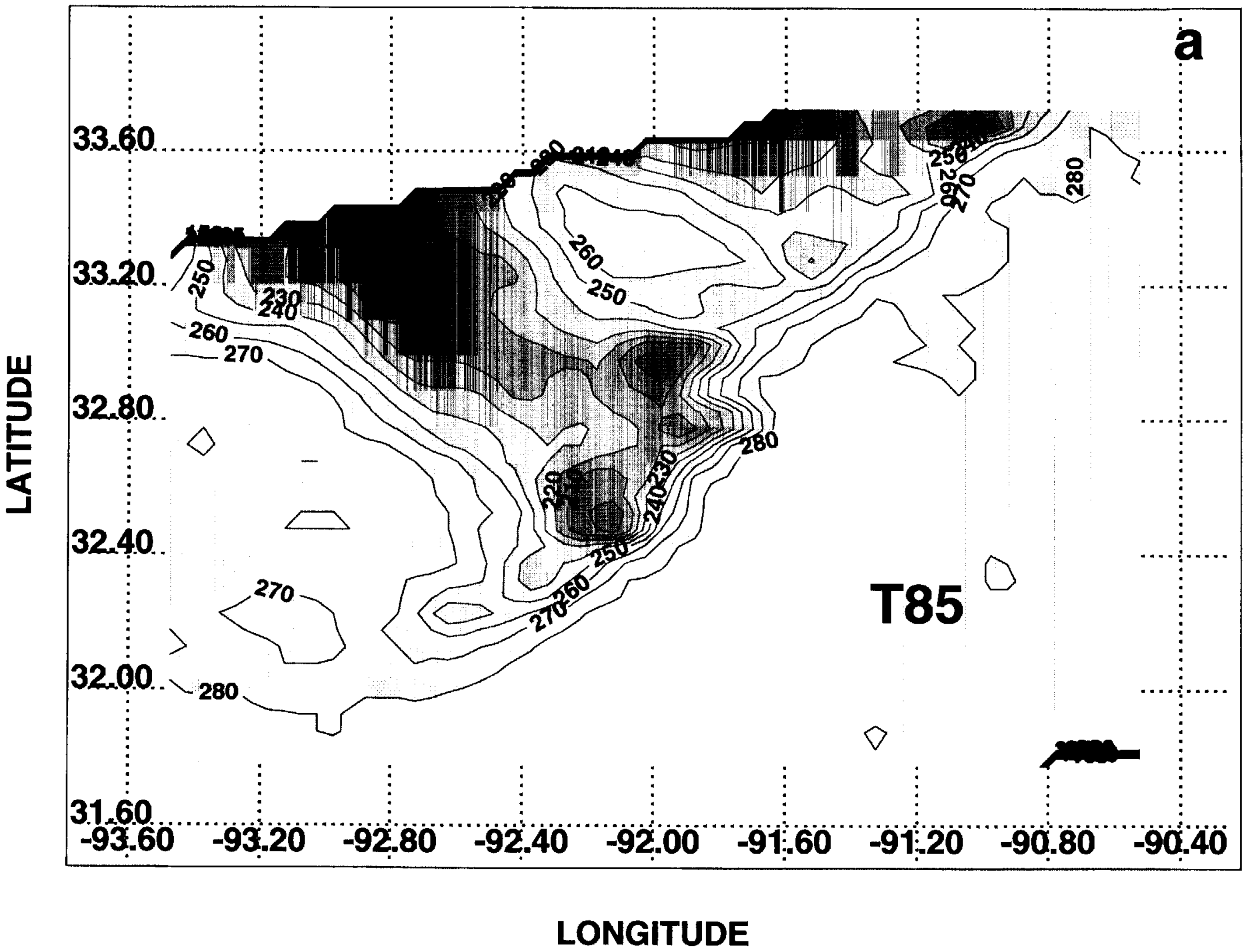
a
T85
LATITUDE
LONGITUDE
33.60
33.20
32.80
32.40
32.00
31.60
-93.60
-93.20
-92.80
-92.40
-92.00
-91.60
-91.20
-90.80
-90.40
220
230
240
250
260
270
280

1a

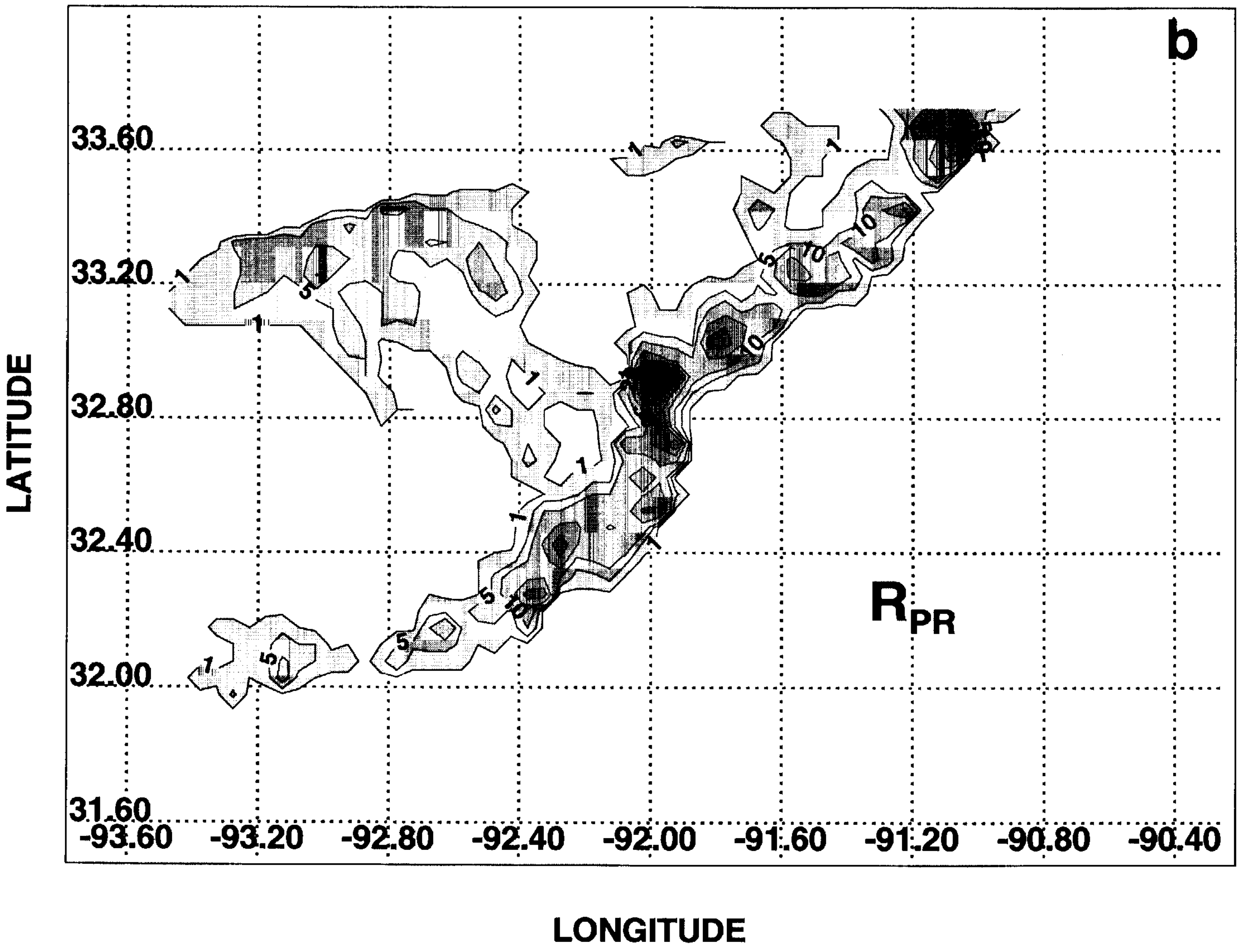
b
R$_{PR}$
33.60
33.20
32.80
32.40
32.00
31.60
-93.60
-93.20
-92.80
-92.40
-92.00
-91.60
-91.20
-90.80
-90.40
LATITUDE
LONGITUDE
1
5
10

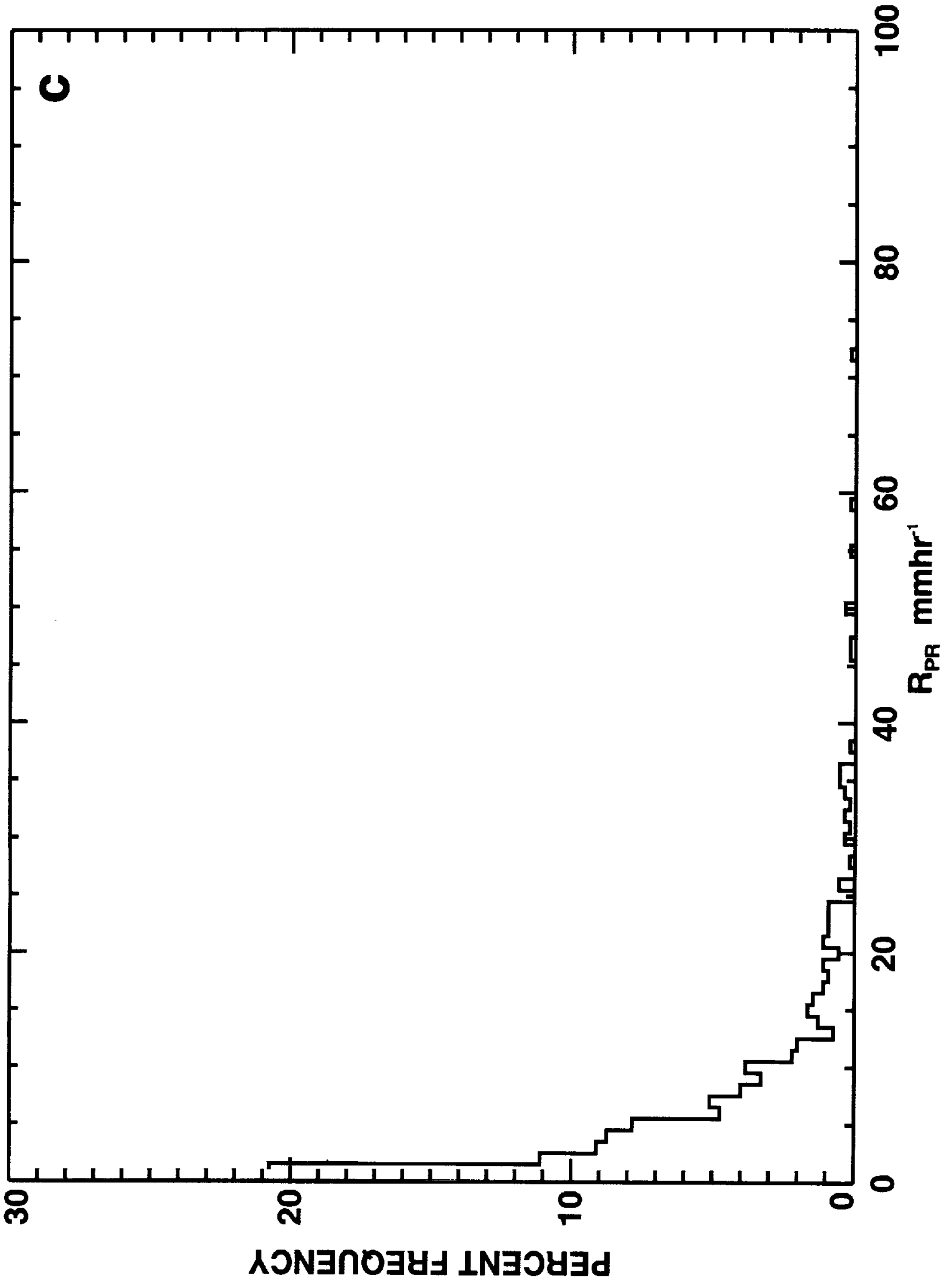

1c

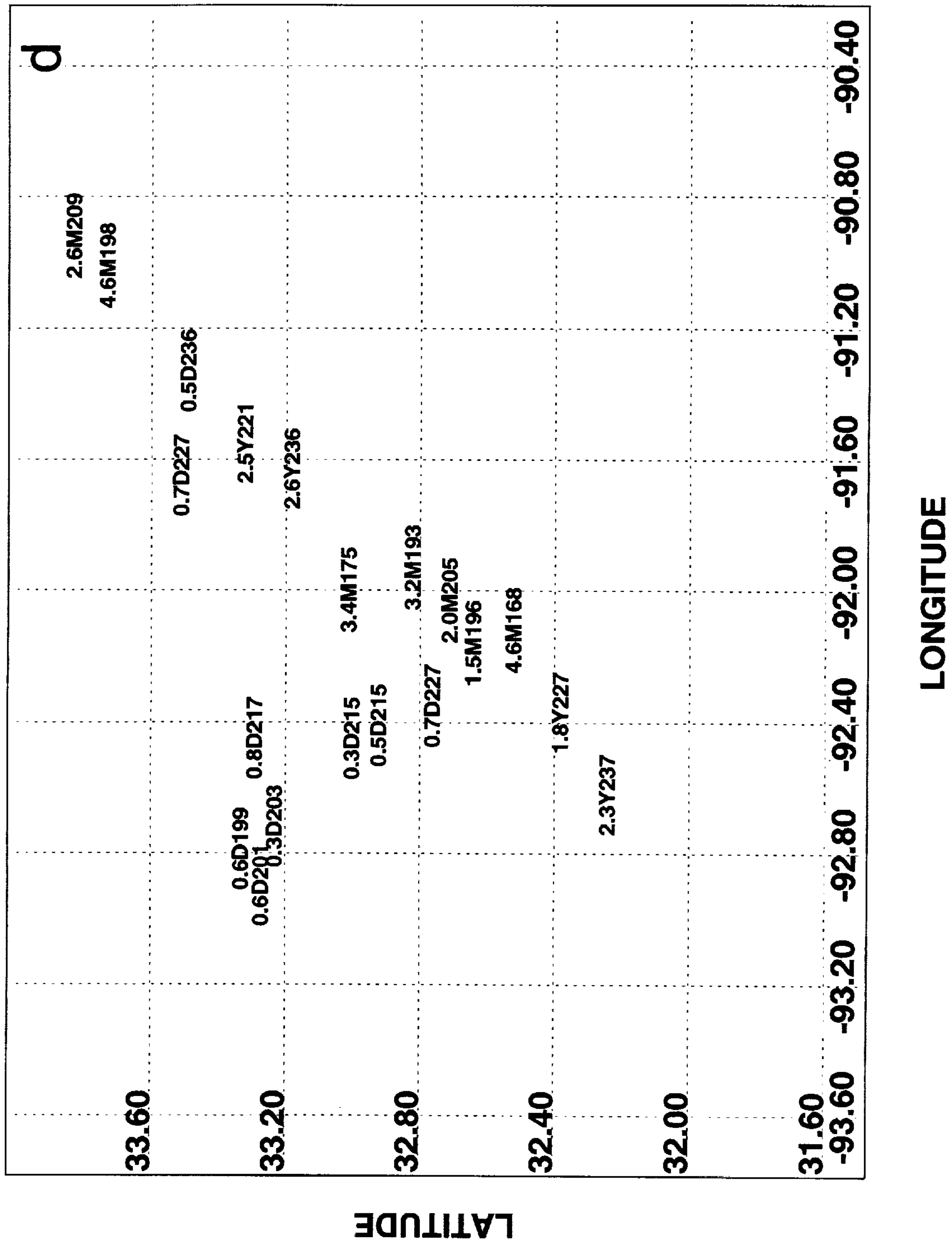
d
LATITUDE
LONGITUDE
33.60
33.20
32.80
32.40
32.00
31.60
-93.60
-93.20
-92.80
-92.40
-92.00
-91.60
-91.20
-90.80
-90.40
2.6M209
4.6M198
0.5D236
0.7D227
2.5Y221
2.6Y236
3.4M175
3.2M193
2.0M205
1.5M196
4.6M168
0.3D215
0.5D215
0.7D227
1.8Y227
0.8D217
2.3Y237
0.6D199
0.6D201
0.3D203

p1

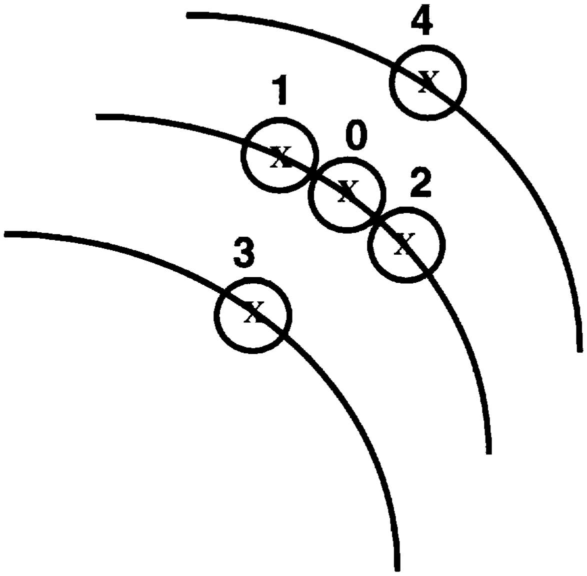

When $T_0 < T_1, T_2, T_3$ and T_4
Then $T_{min} = T_0$

$$\overline{\frac{dT}{dr}} \propto \frac{A(T_1 + T_2) + B(T_3 + T_4) - 4T_0}{4}$$

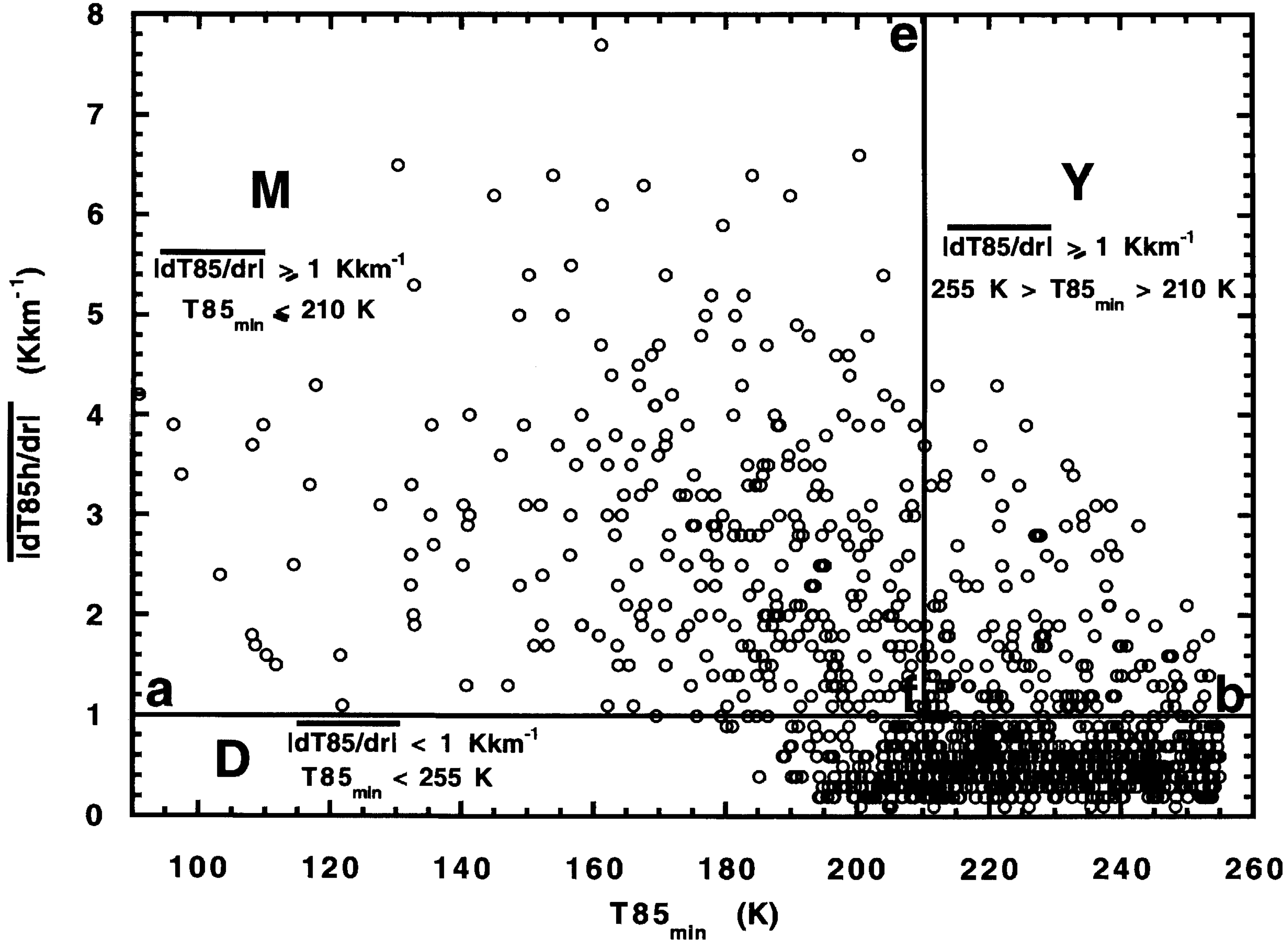
M
$\overline{|dT85/dr|} \geq 1$ Kkm^{-1}
$T85_{min} \leq 210$ K
Y
$\overline{|dT85/dr|} \geq 1$ Kkm^{-1}
255 K > $T85_{min}$ > 210 K
D
$\overline{|dT85/dr|} < 1$ Kkm^{-1}
$T85_{min} < 255$ K
a
b
e
f
$\overline{|dT85h/dr|}$ (Kkm^{-1})
0
1
2
3
4
5
6
7
8
100
120
140
160
180
200
220
240
260
$T85_{min}$ (K)

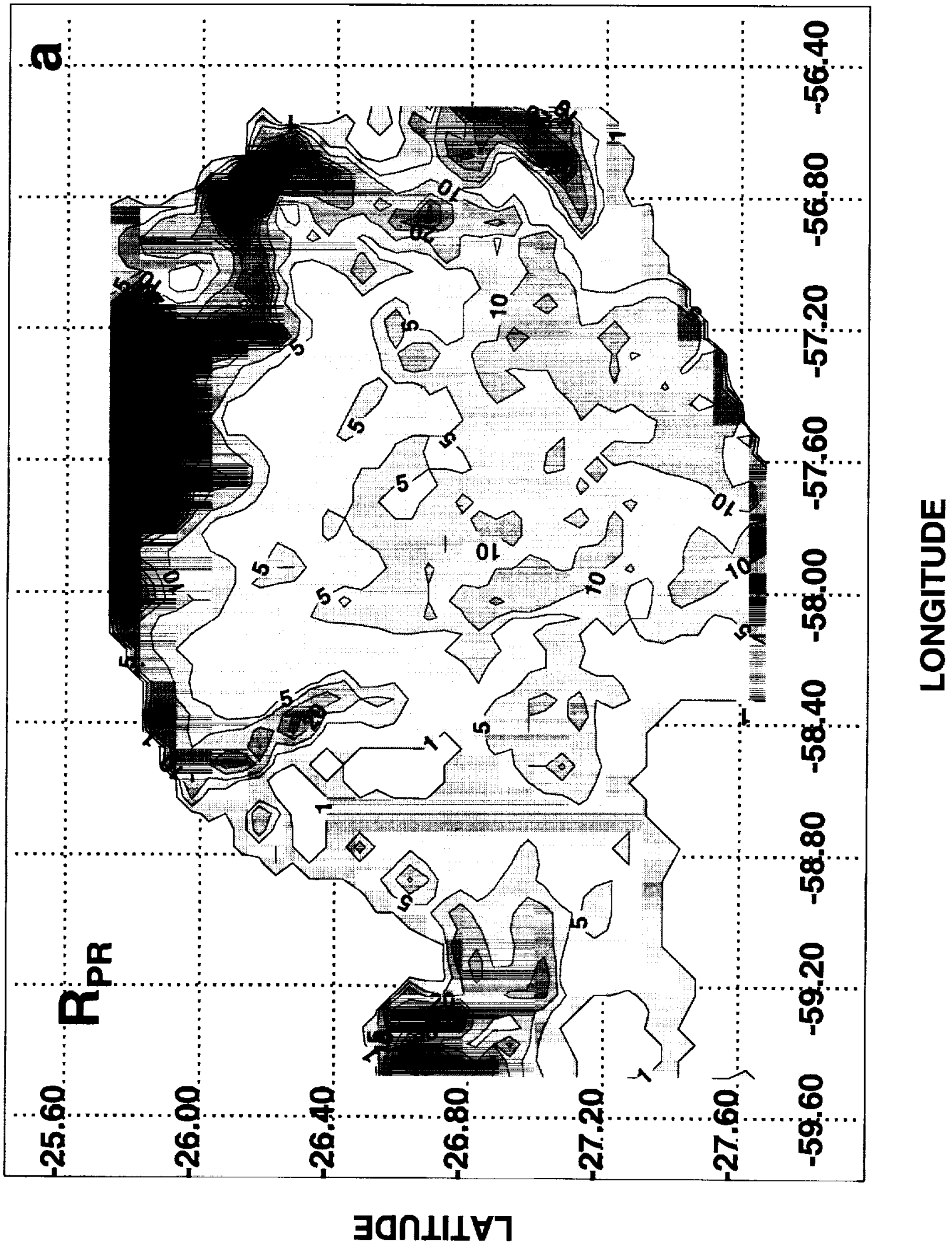
R_PR
a
-25.60
-26.00
-26.40
-26.80
-27.20
-27.60
-59.60
-59.20
-58.80
-58.40
-58.00
-57.60
-57.20
-56.80
-56.40
LATITUDE
LONGITUDE
1
5
10
20

4a

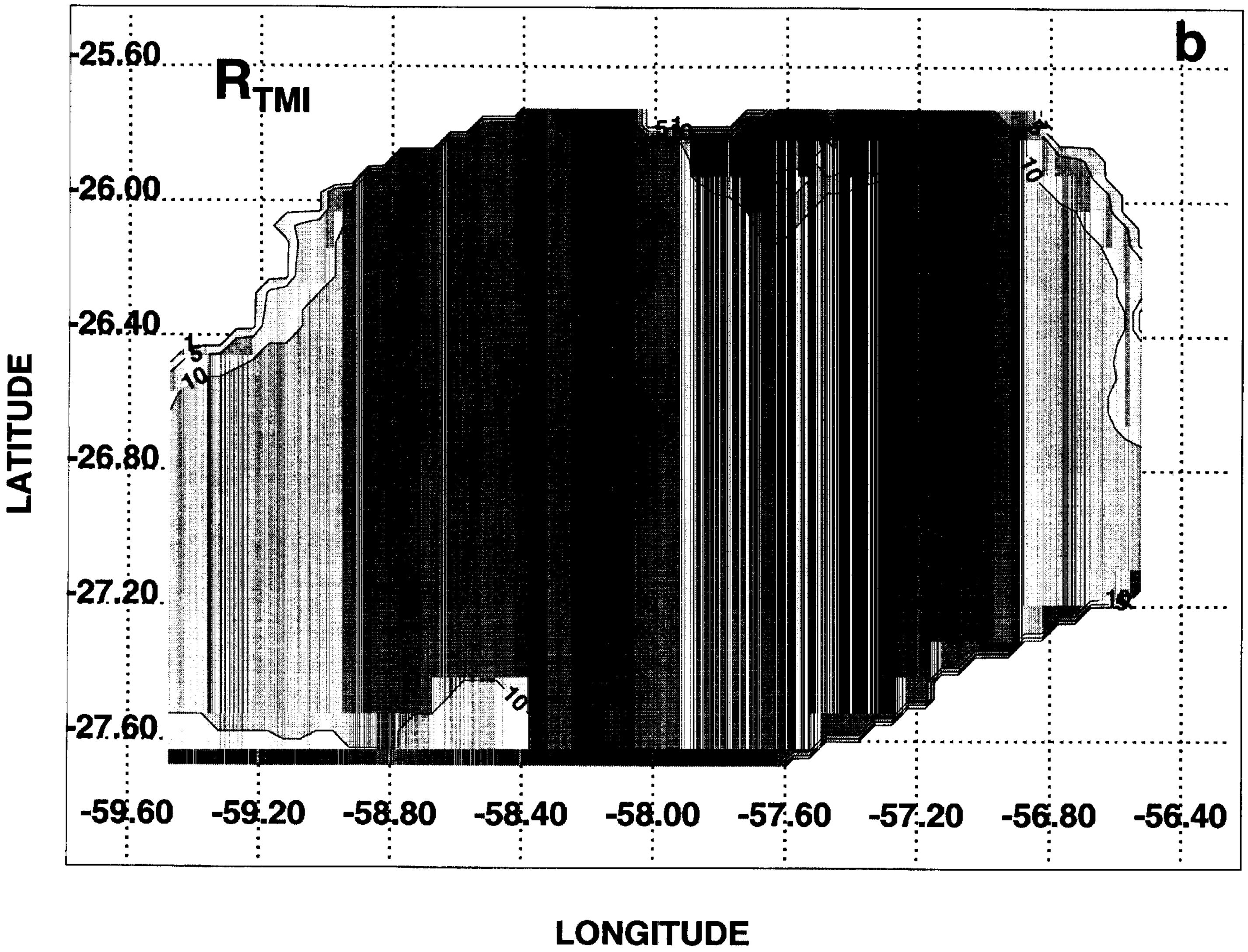
R_TMI
b
-25.60
-26.00
-26.40
-26.80
-27.20
-27.60
-59.60
-59.20
-58.80
-58.40
-58.00
-57.60
-57.20
-56.80
-56.40
5
10
LATITUDE
LONGITUDE

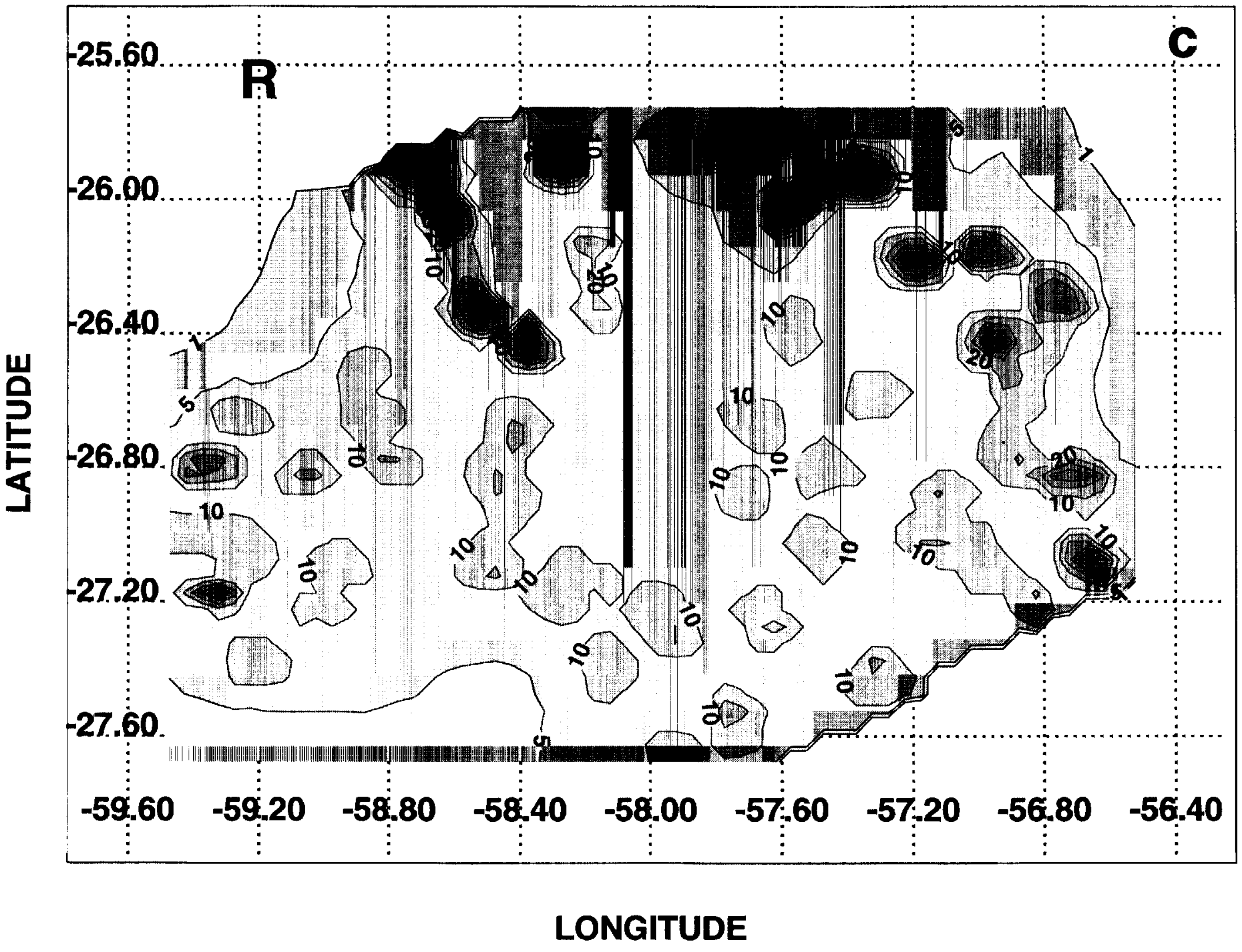
C
R
-25.60
-26.00
-26.40
-26.80
-27.20
-27.60
-59.60
-59.20
-58.80
-58.40
-58.00
-57.60
-57.20
-56.80
-56.40
LATITUDE
LONGITUDE
1
5
10
20

4c

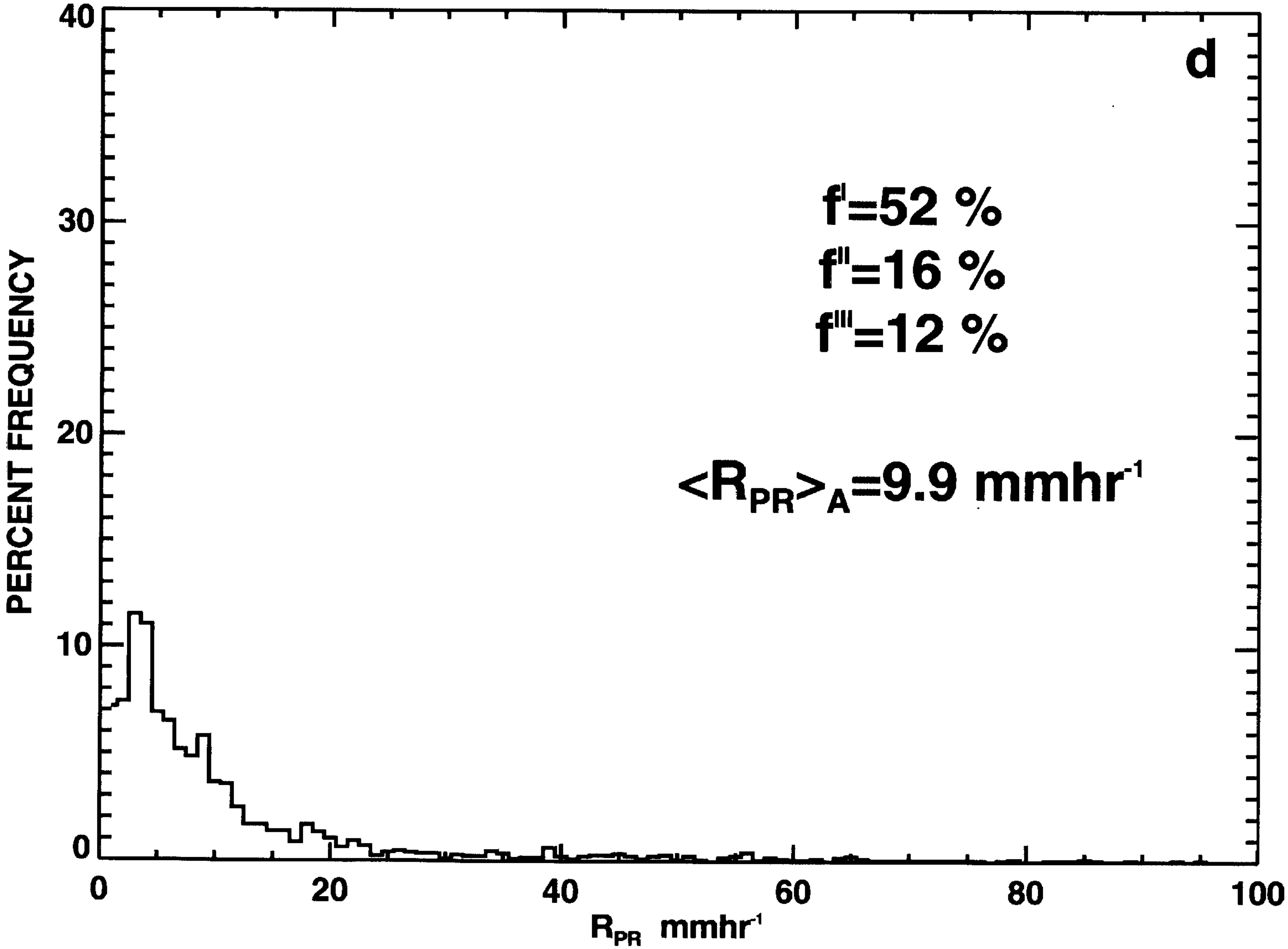
d
f^{I}=52 %
f^{II}=16 %
f^{III}=12 %
<R$_{PR}$>$_{A}$=9.9 mmhr^{-1}
PERCENT FREQUENCY
0
10
20
30
40
0
20
40
60
80
100
R$_{PR}$ mmhr^{-1}

4d

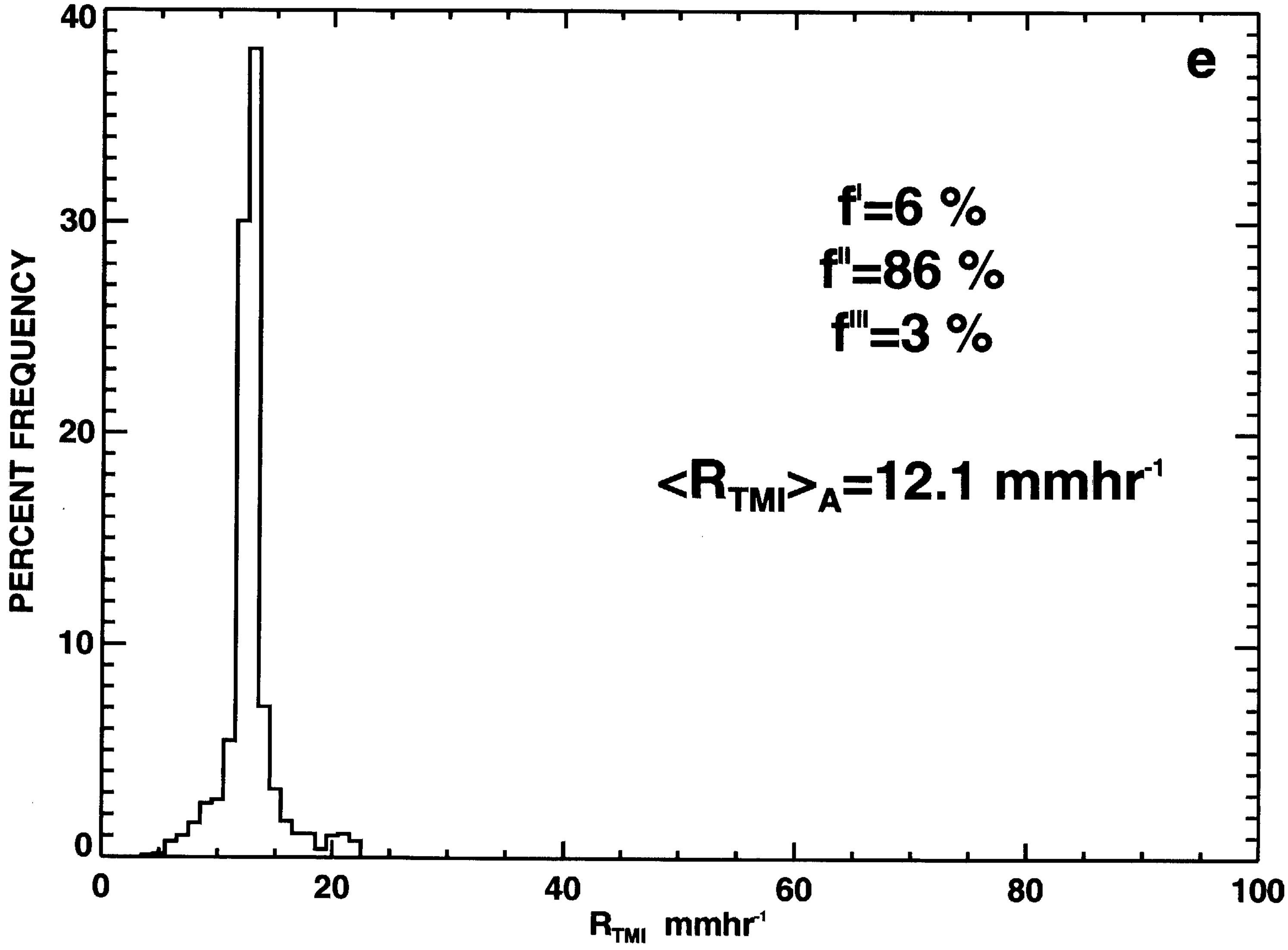
e
f^{I}=6 %
f^{II}=86 %
f^{III}=3 %
$<R_{TMI}>_A$=12.1 $mmhr^{-1}$
PERCENT FREQUENCY
0
10
20
30
40
0
20
40
60
80
100
R_{TMI} $mmhr^{-1}$

4e

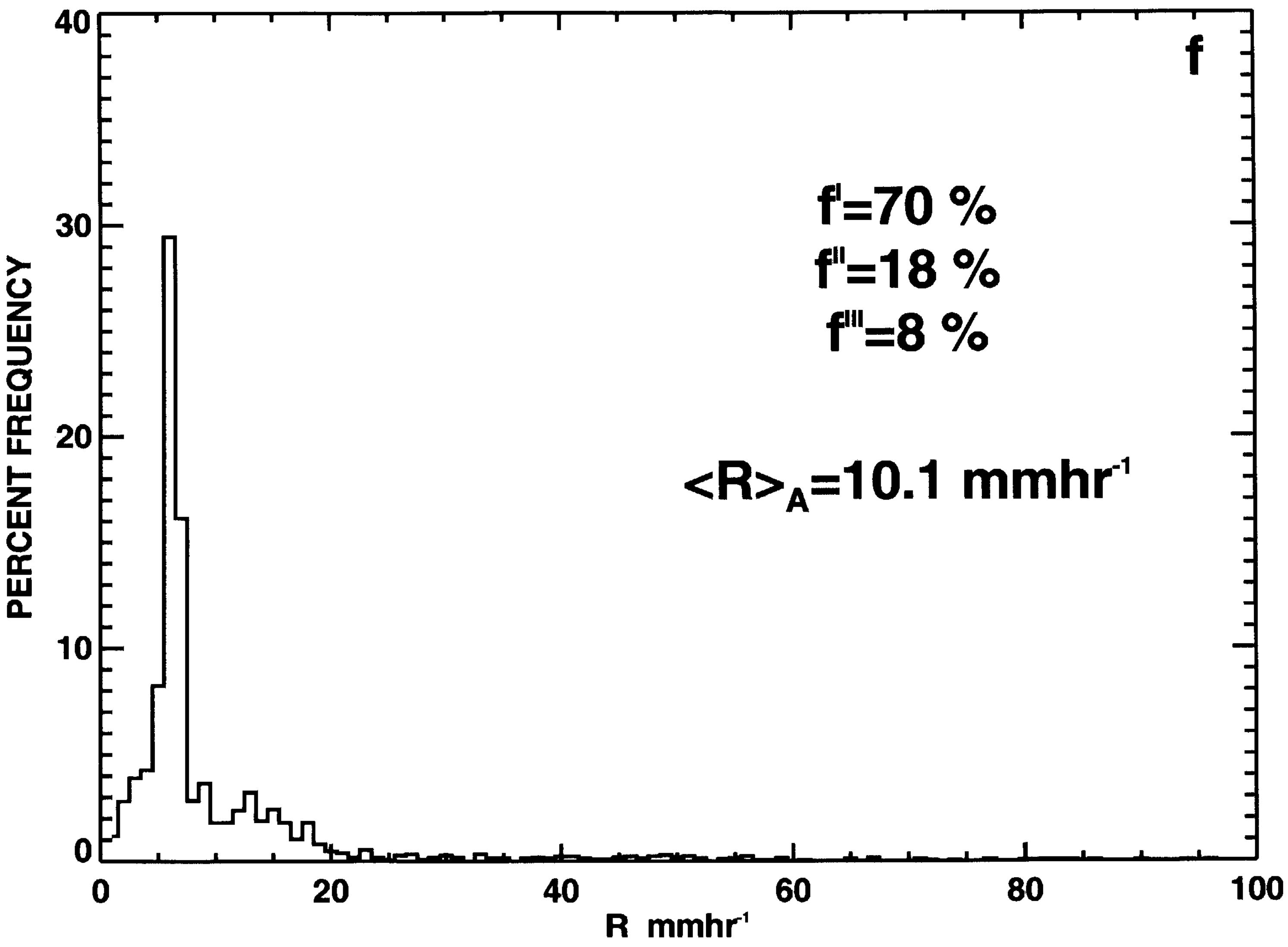
f
f^{I}=70 %
f^{II}=18 %
f^{III}=8 %
$<R>_A$=10.1 mmhr^{-1}
PERCENT FREQUENCY
0
10
20
30
40
0
20
40
60
80
100
R mmhr^{-1}

4F

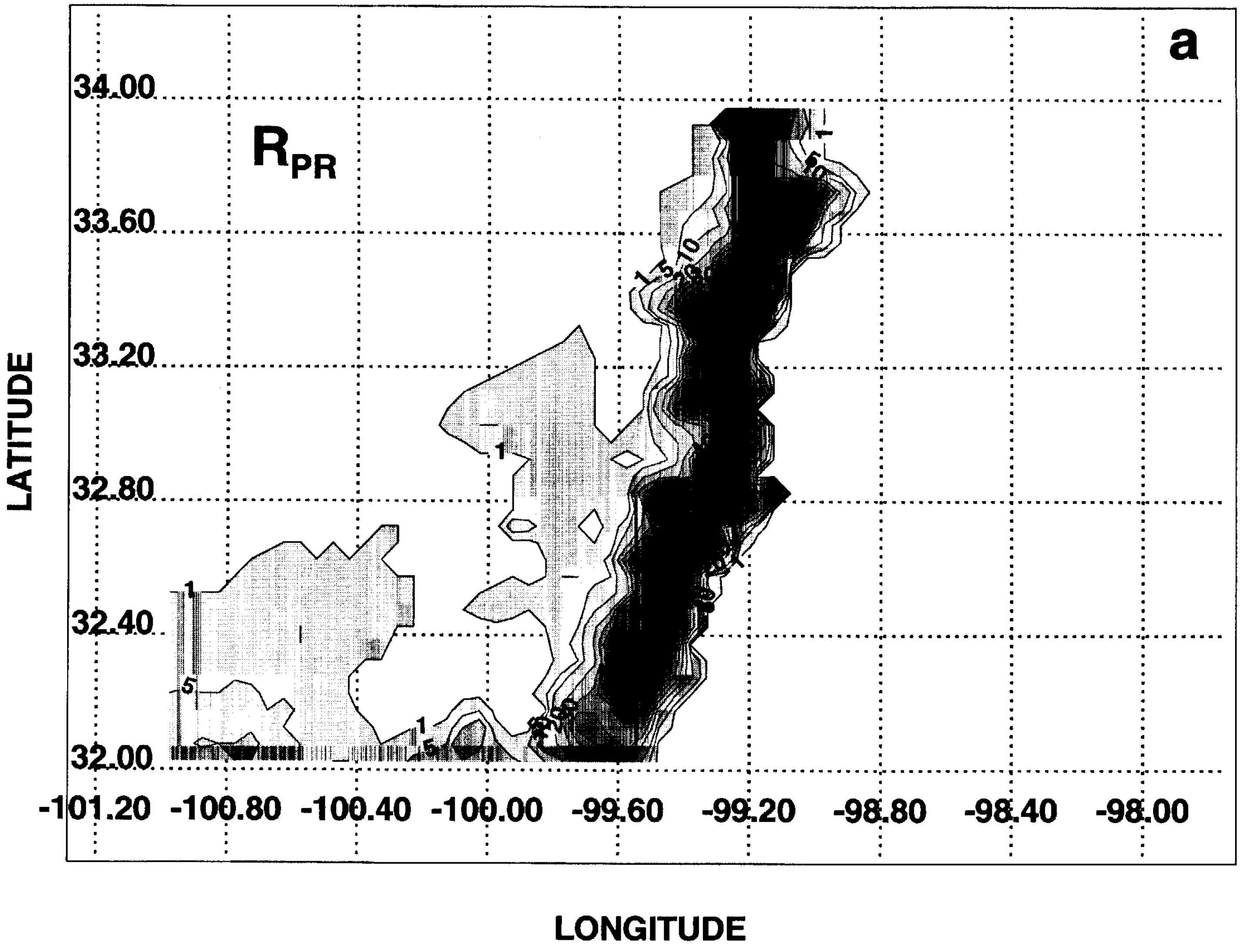
a
R_PR
34.00
33.60
33.20
32.80
32.40
32.00
-101.20
-100.80
-100.40
-100.00
-99.60
-99.20
-98.80
-98.40
-98.00
LATITUDE
LONGITUDE
1
5
10
50
100

5a

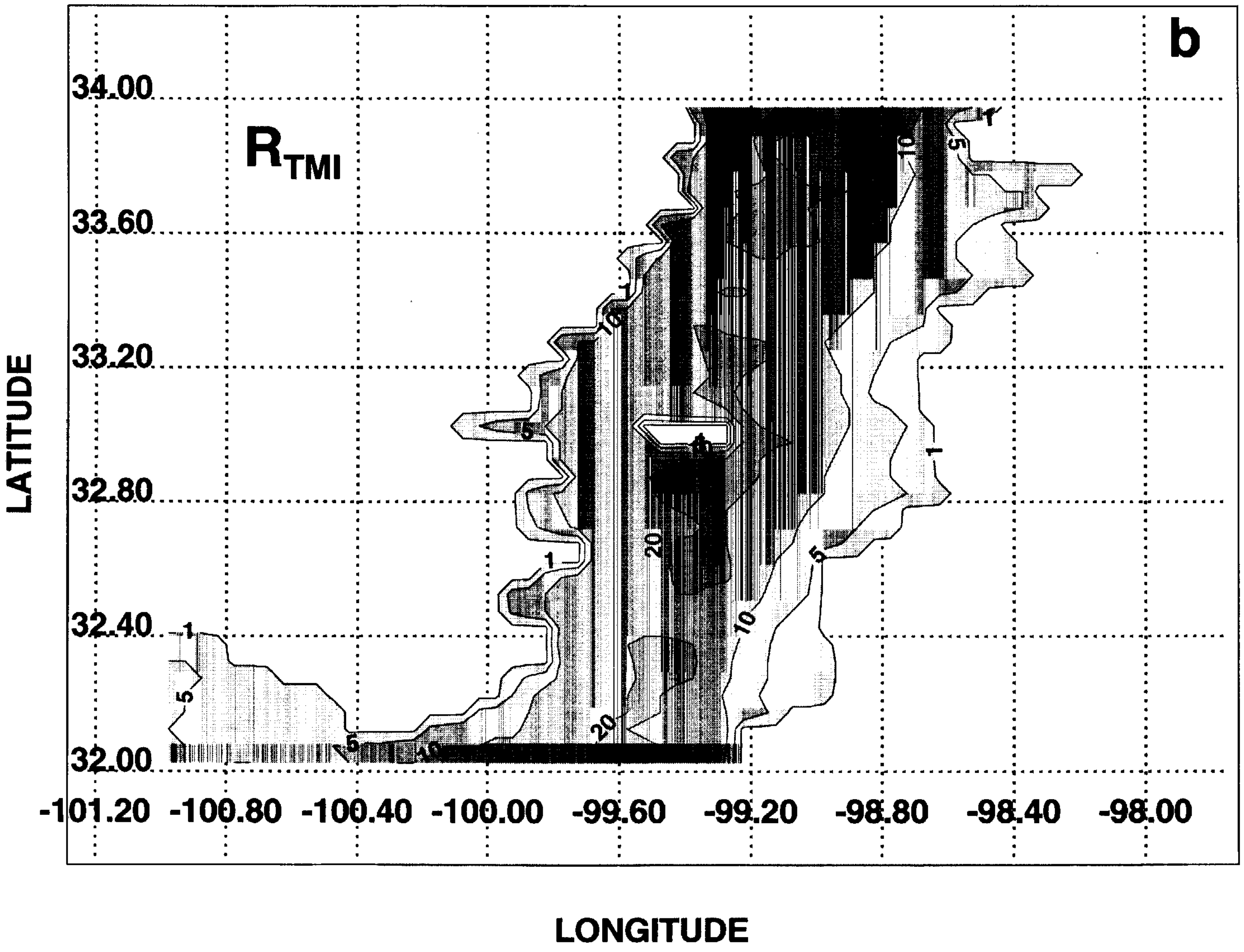
b
R_{TMI}
34.00
33.60
33.20
32.80
32.40
32.00
LATITUDE
-101.20
-100.80
-100.40
-100.00
-99.60
-99.20
-98.80
-98.40
-98.00
LONGITUDE
1
5
10
20

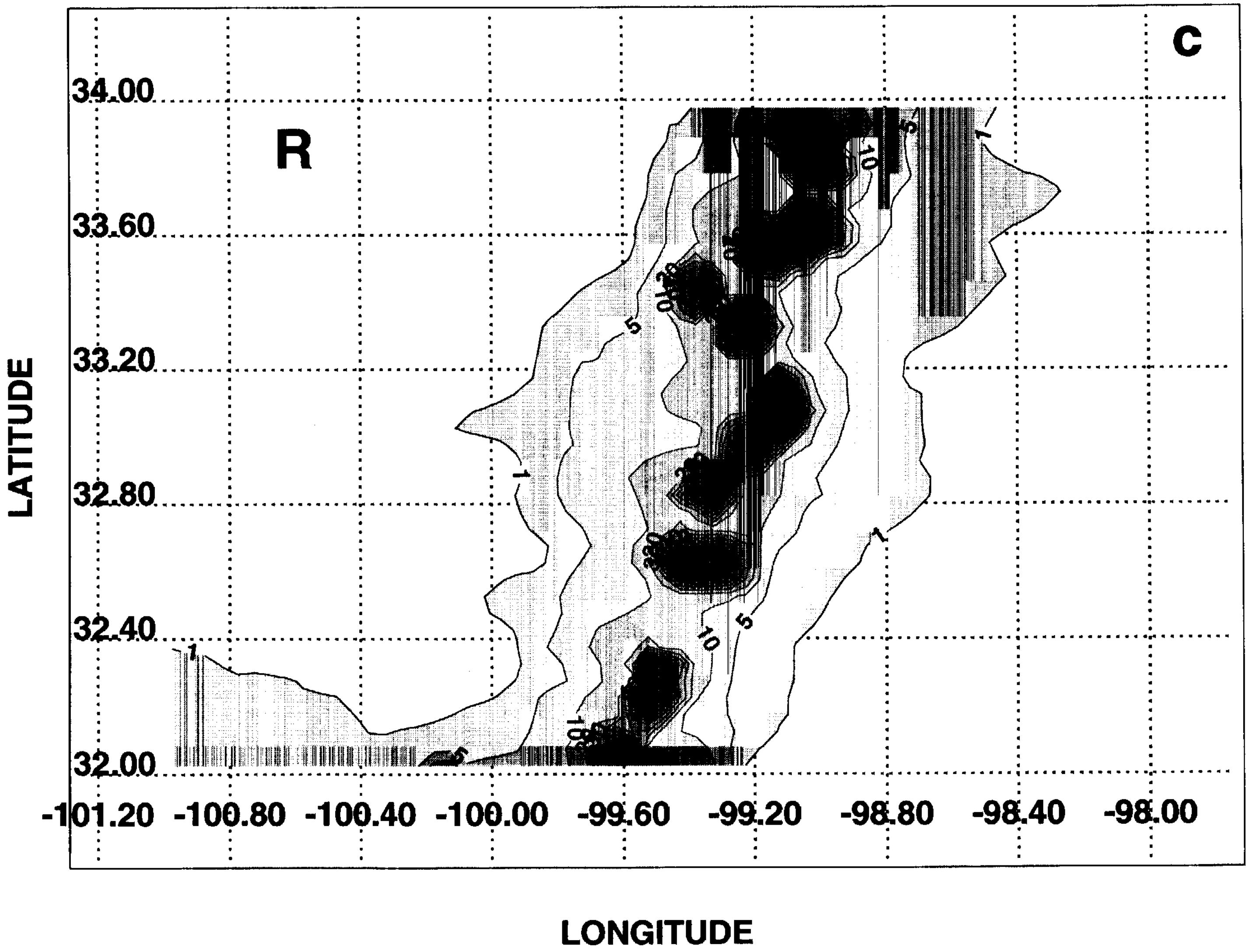
c
R
LATITUDE
34.00
33.60
33.20
32.80
32.40
32.00
LONGITUDE
-101.20
-100.80
-100.40
-100.00
-99.60
-99.20
-98.80
-98.40
-98.00
1
5
10
20
30

5c

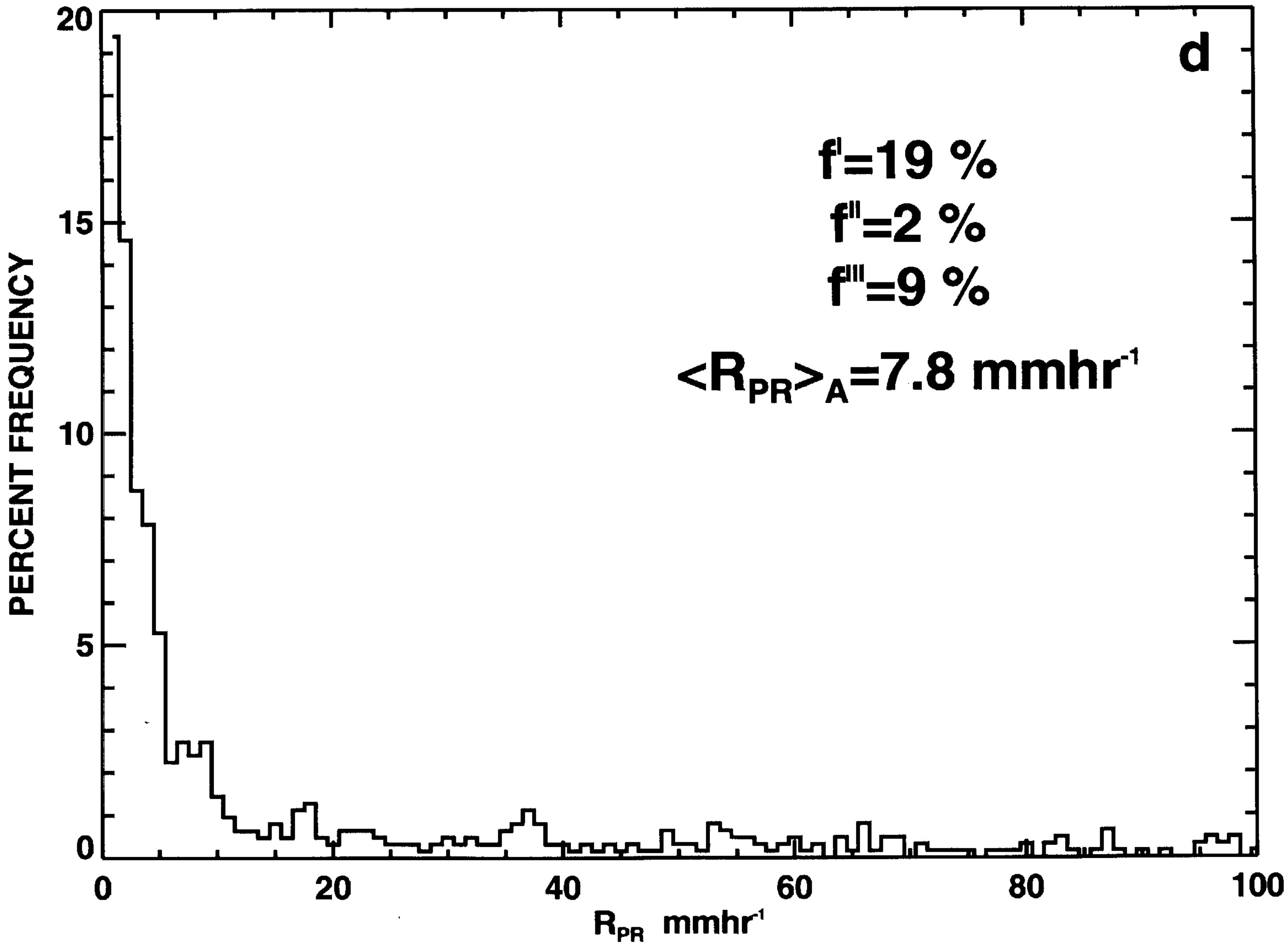
d
f^{I}=19 %
f^{II}=2 %
f^{III}=9 %
$<R_{PR}>_A$=7.8 mmhr^{-1}
PERCENT FREQUENCY
0
5
10
15
20
0
20
40
60
80
100
R_{PR} mmhr^{-1}

5d

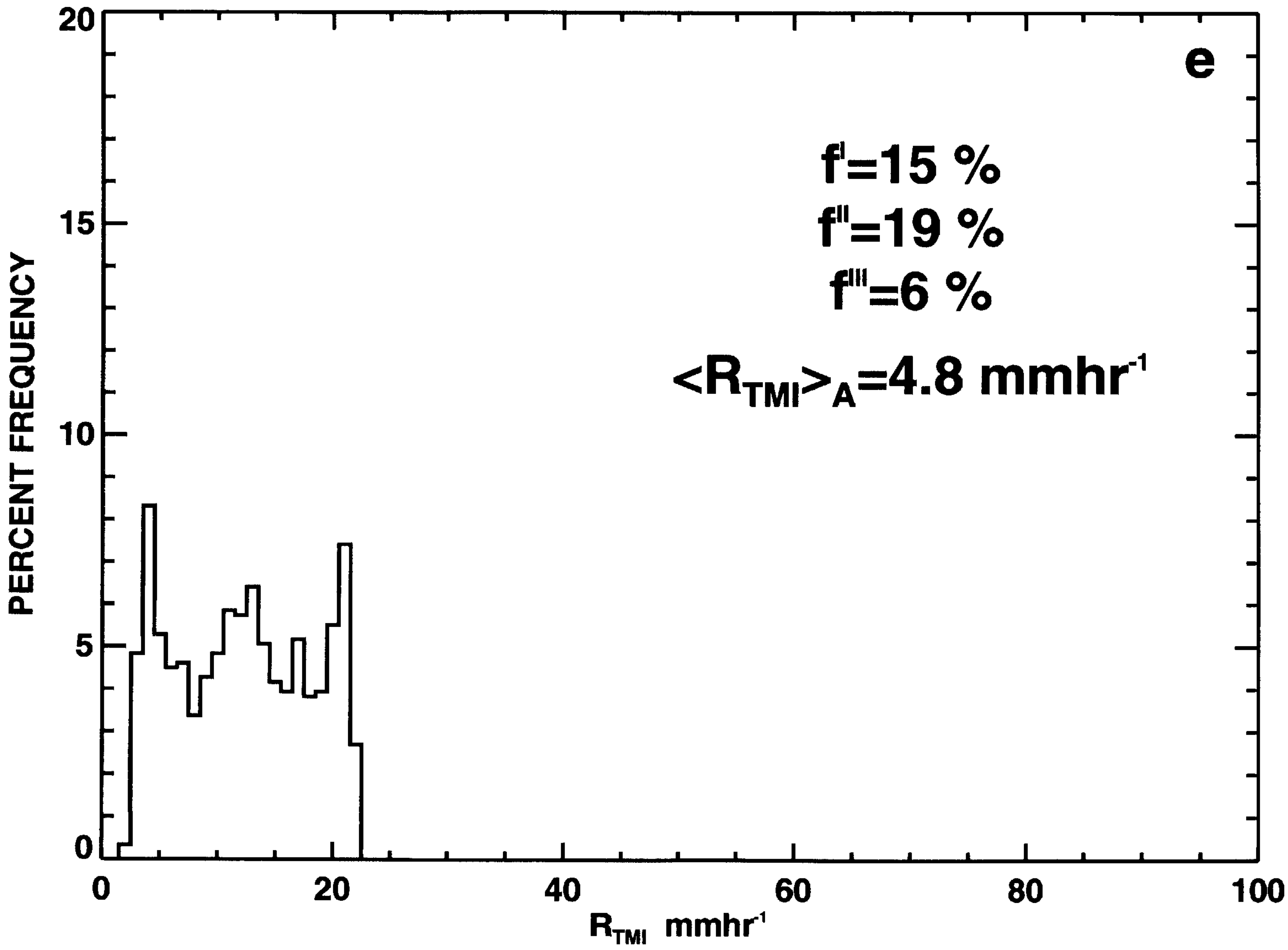
e
$f^{I}=15$ %
$f^{II}=19$ %
$f^{III}=6$ %
$\langle R_{TMI} \rangle_A=4.8$ $mmhr^{-1}$
PERCENT FREQUENCY
0
5
10
15
20
0
20
40
60
80
100
R_{TMI} $mmhr^{-1}$

1 5e

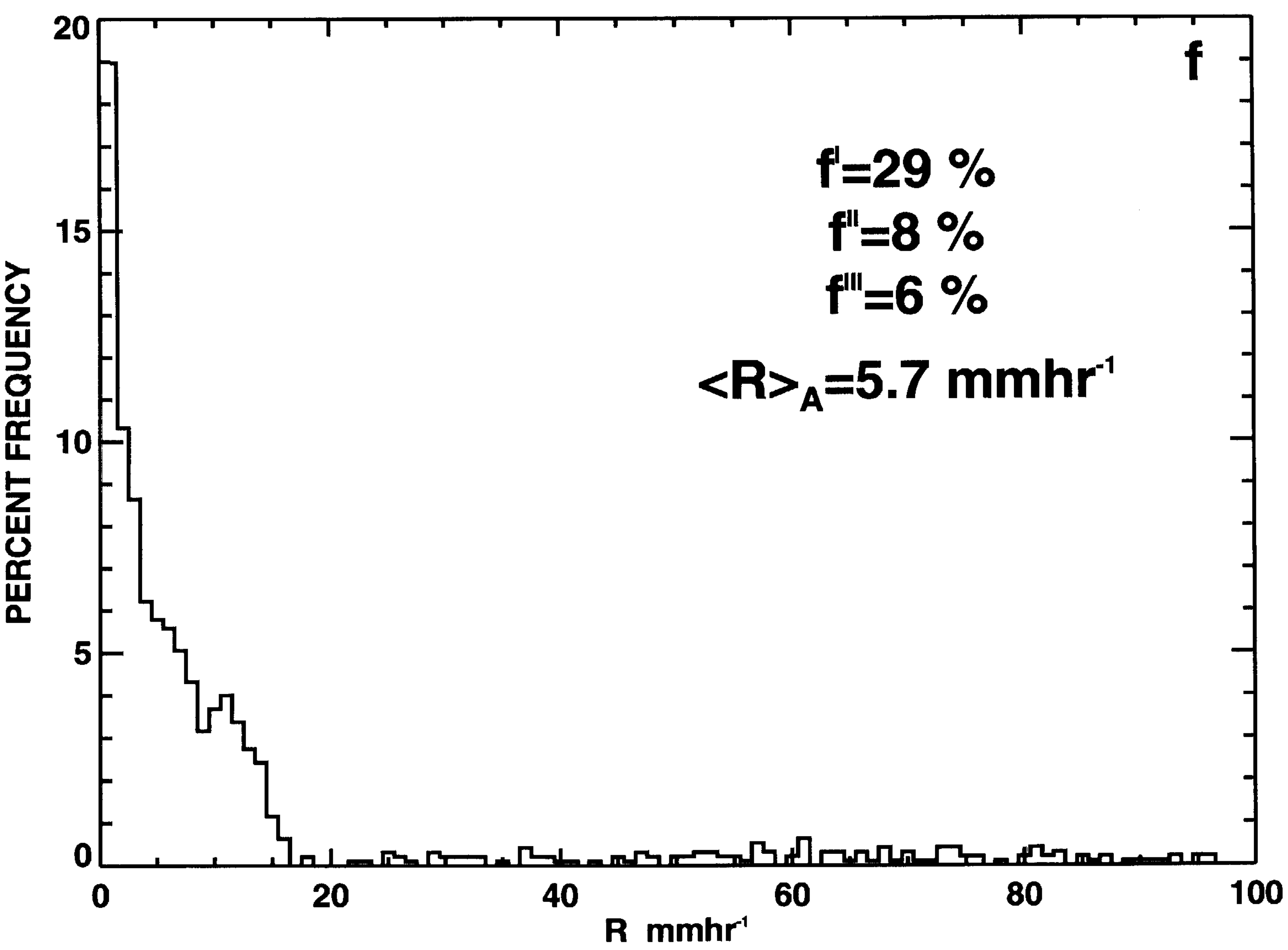
f
f^{I}=29 %
f^{II}=8 %
f^{III}=6 %
$\langle R\rangle_A$=5.7 mmhr^{-1}
PERCENT FREQUENCY
20
15
10
5
0
0
20
40
60
80
100
R mmhr^{-1}

5f

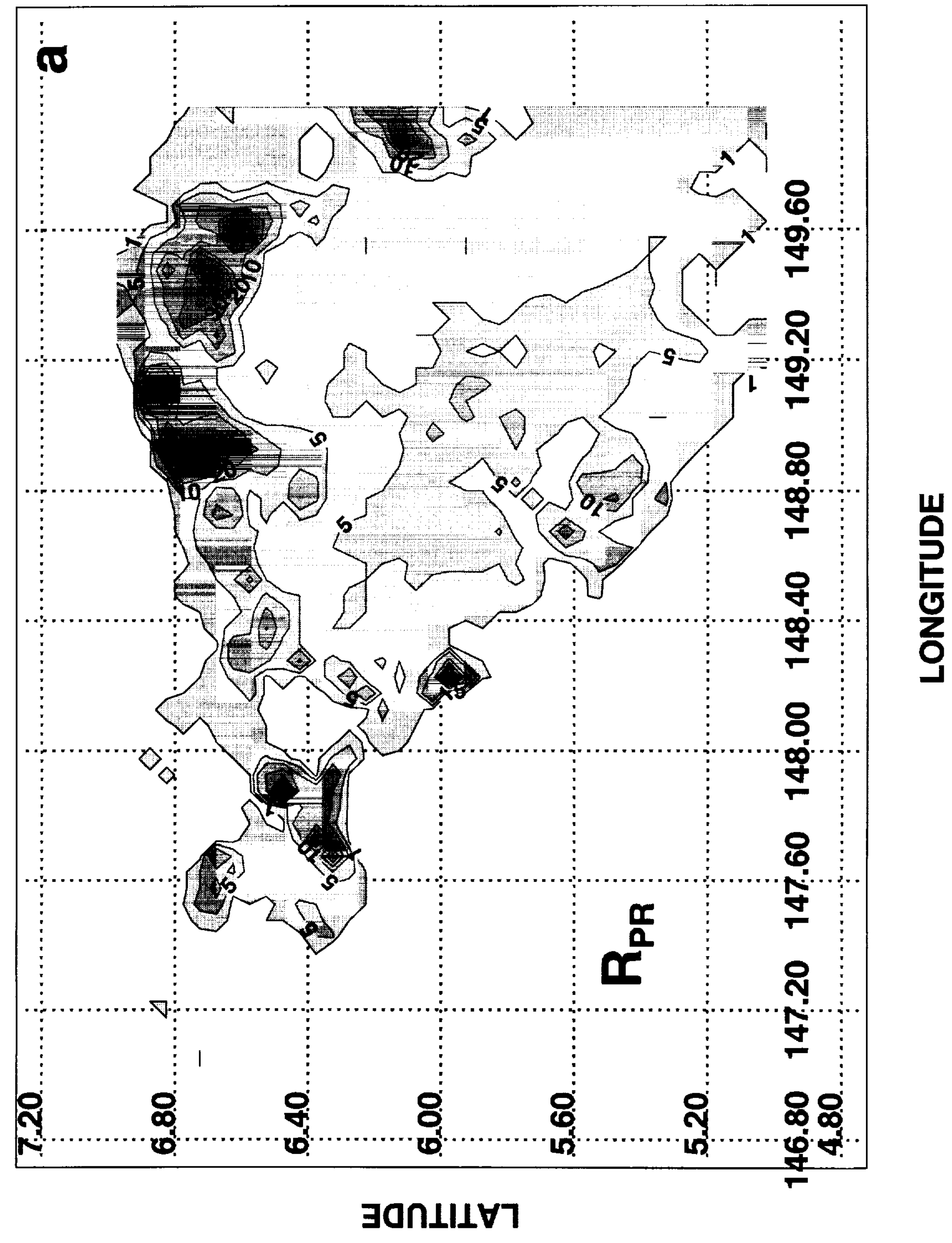
a
R_PR
LATITUDE
LONGITUDE
7.20
6.80
6.40
6.00
5.60
5.20
4.80
146.80
147.20
147.60
148.00
148.40
148.80
149.20
149.60
1
5
10
15
20

6a

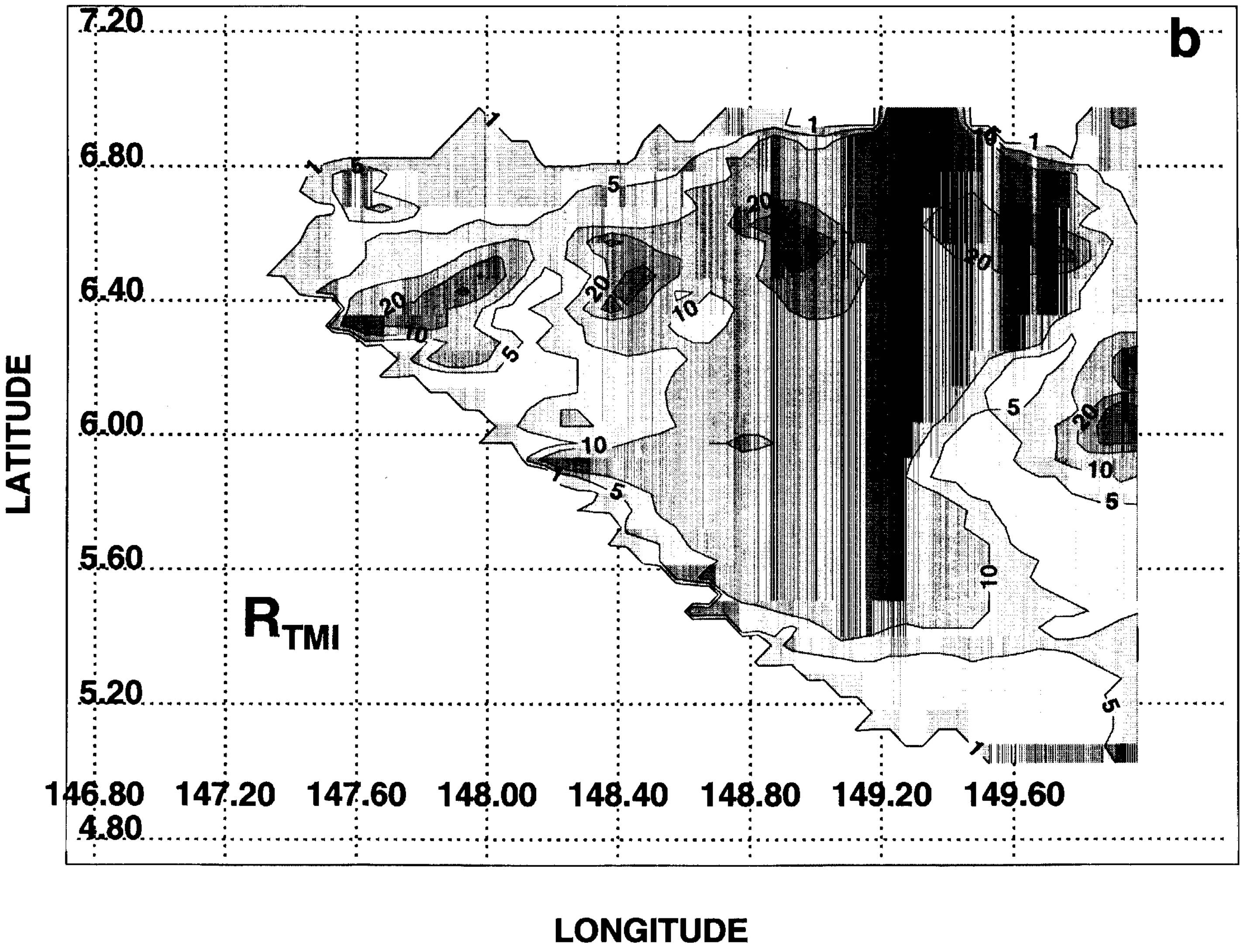
b
R_TMI
LATITUDE
LONGITUDE
7.20
6.80
6.40
6.00
5.60
5.20
4.80
146.80
147.20
147.60
148.00
148.40
148.80
149.20
149.60
1
5
10
20

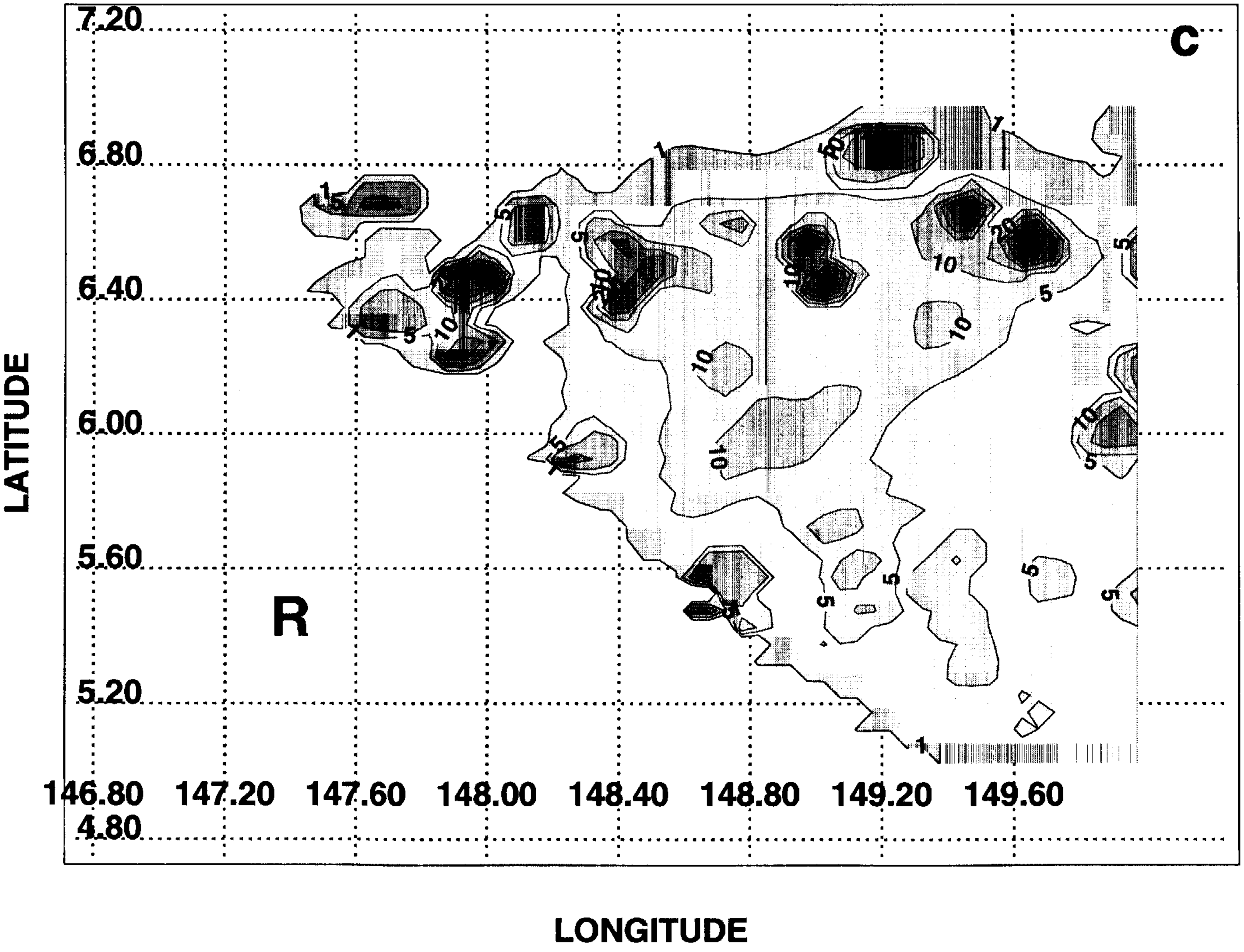
C
R
LATITUDE
7.20
6.80
6.40
6.00
5.60
5.20
4.80
LONGITUDE
146.80
147.20
147.60
148.00
148.40
148.80
149.20
149.60
1
5
10
20

6c

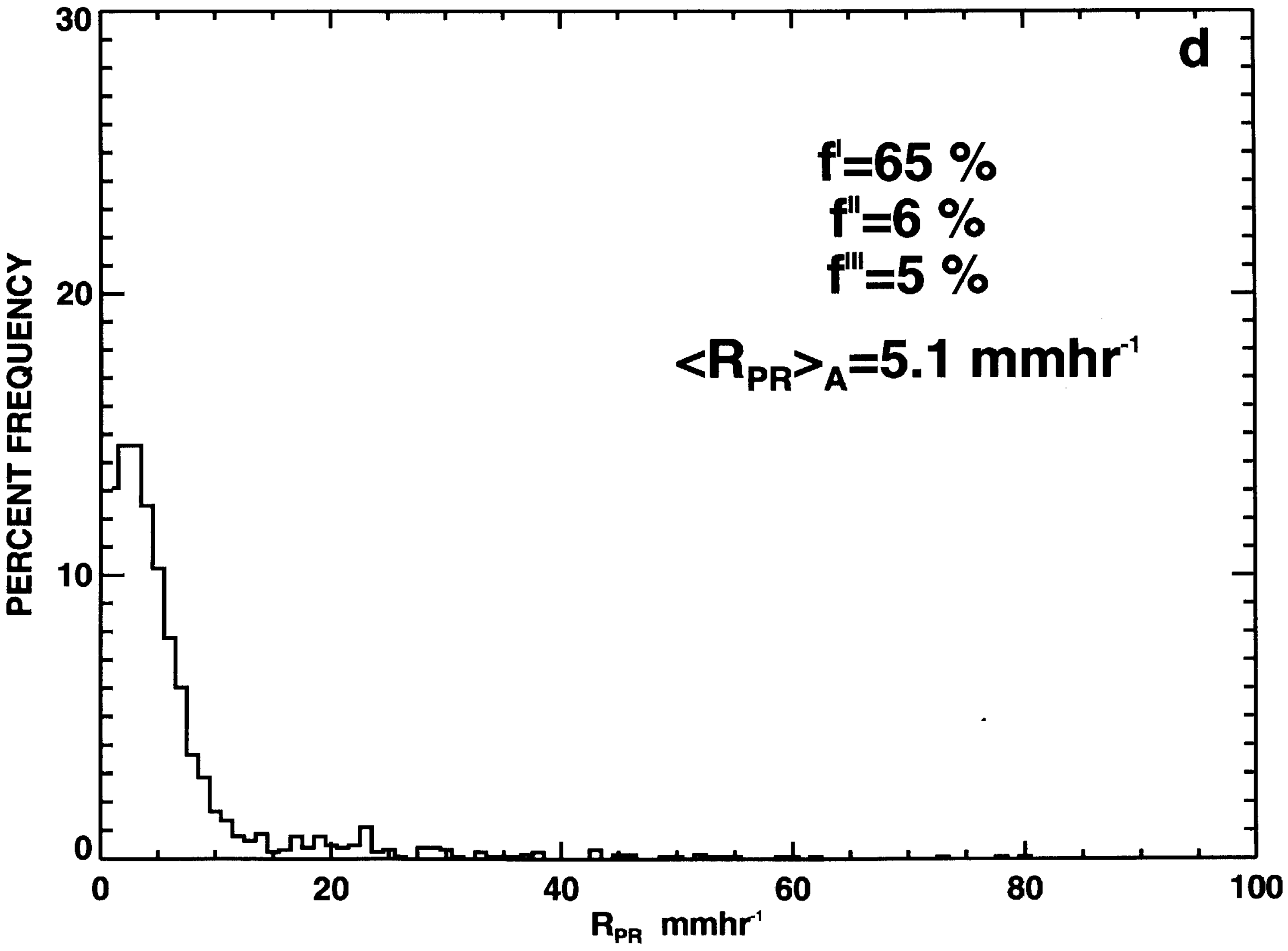
d
f^{I}=65 %
f^{II}=6 %
f^{III}=5 %
$<R_{PR}>_A$=5.1 mmhr^{-1}
PERCENT FREQUENCY
0
10
20
30
0
20
40
60
80
100
R_{PR} mmhr^{-1}

6d

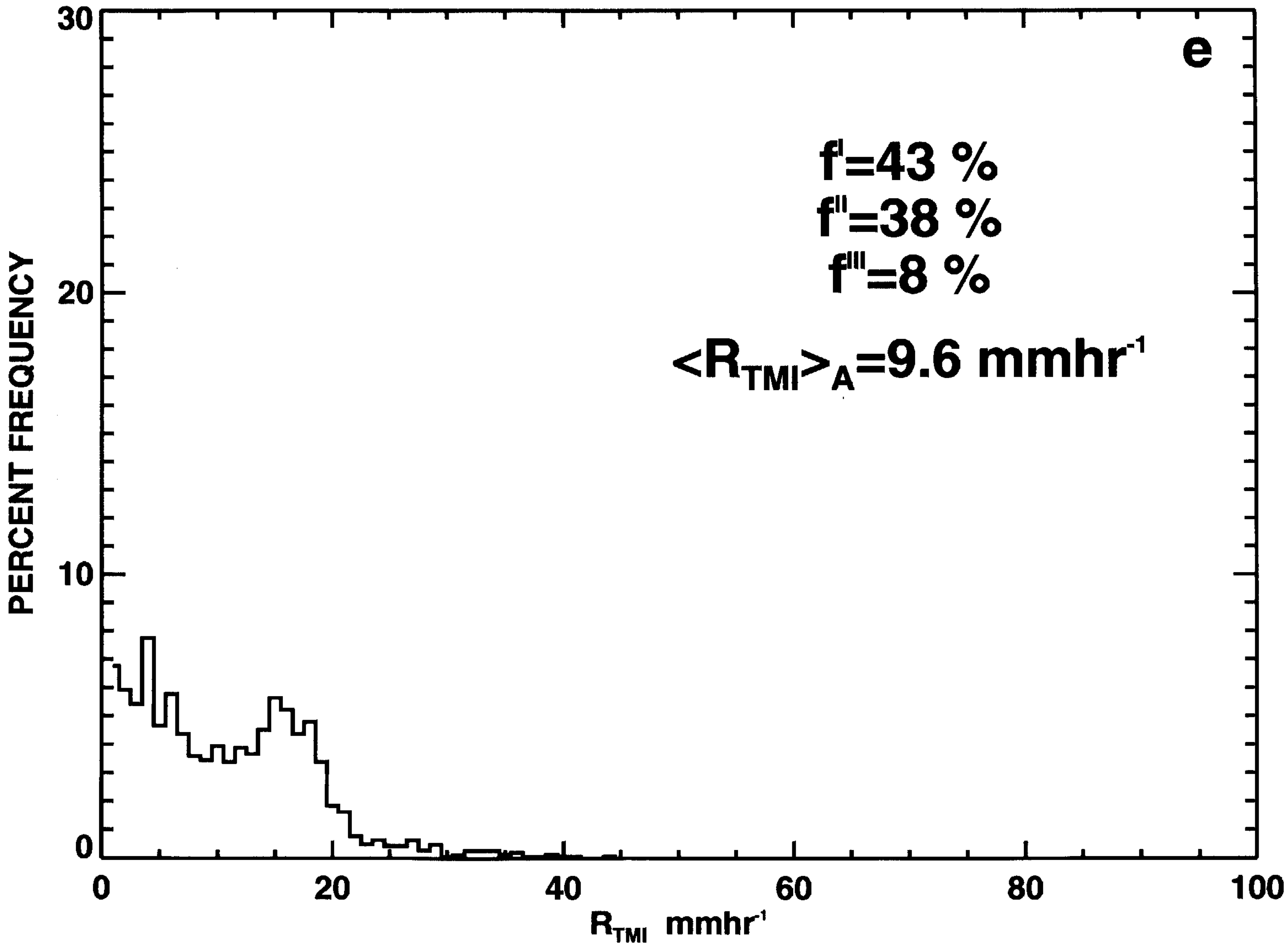
e
f^{I}=43 %
f^{II}=38 %
f^{III}=8 %
$<R_{TMI}>_A$=9.6 $mmhr^{-1}$
PERCENT FREQUENCY
30
20
10
0
0
20
40
60
80
100
R_{TMI} $mmhr^{-1}$

6e

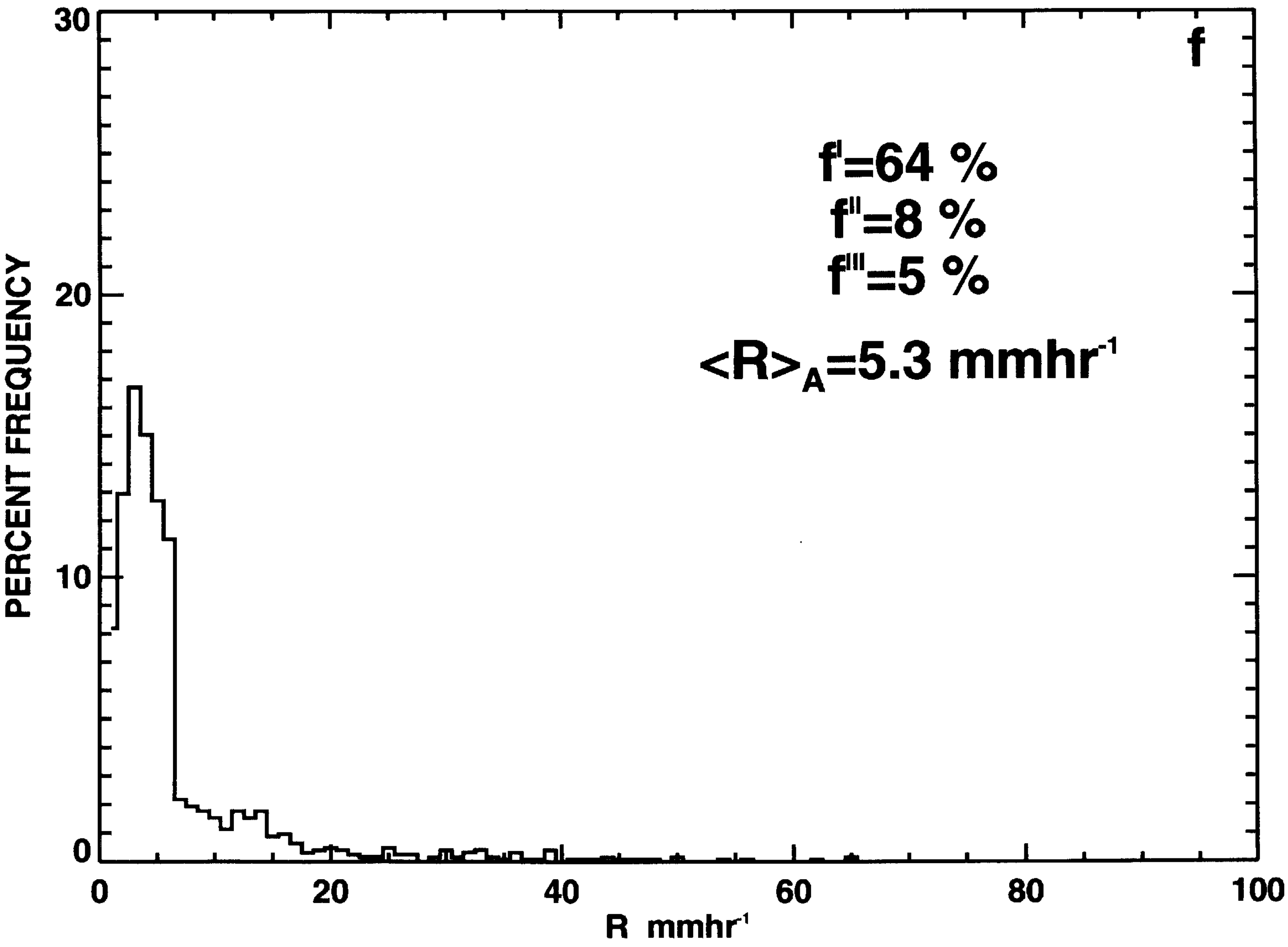
f
$f^{I}=64$ %
$f^{II}=8$ %
$f^{III}=5$ %
$\langle R \rangle_A=5.3$ mmhr^{-1}
PERCENT FREQUENCY
0
10
20
30
0
20
40
60
80
100
R mmhr^{-1}

6f

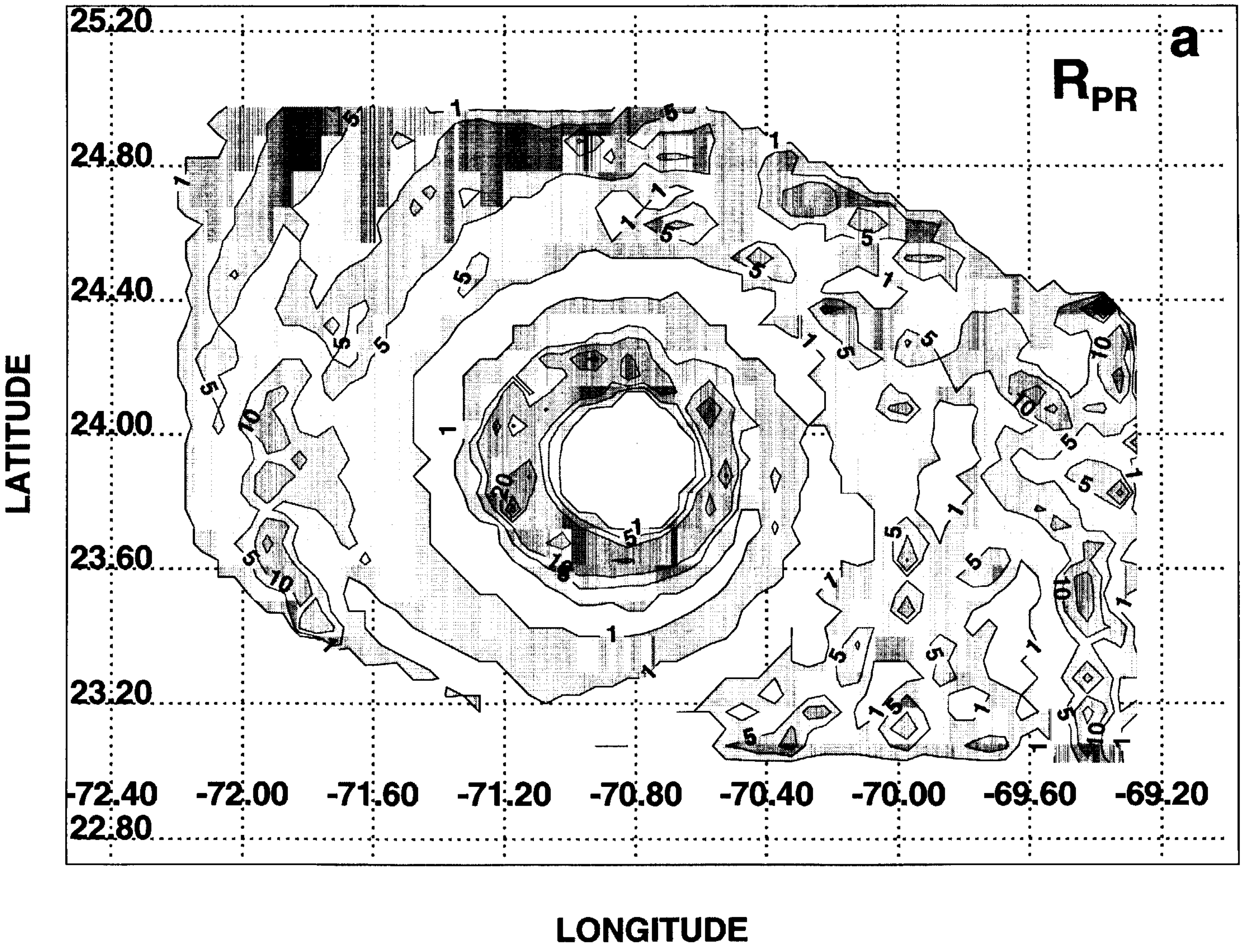
a
R_{PR}
LATITUDE
25.20
24.80
24.40
24.00
23.60
23.20
22.80
-72.40
-72.00
-71.60
-71.20
-70.80
-70.40
-70.00
-69.60
-69.20
LONGITUDE
1
5
10
20

7a

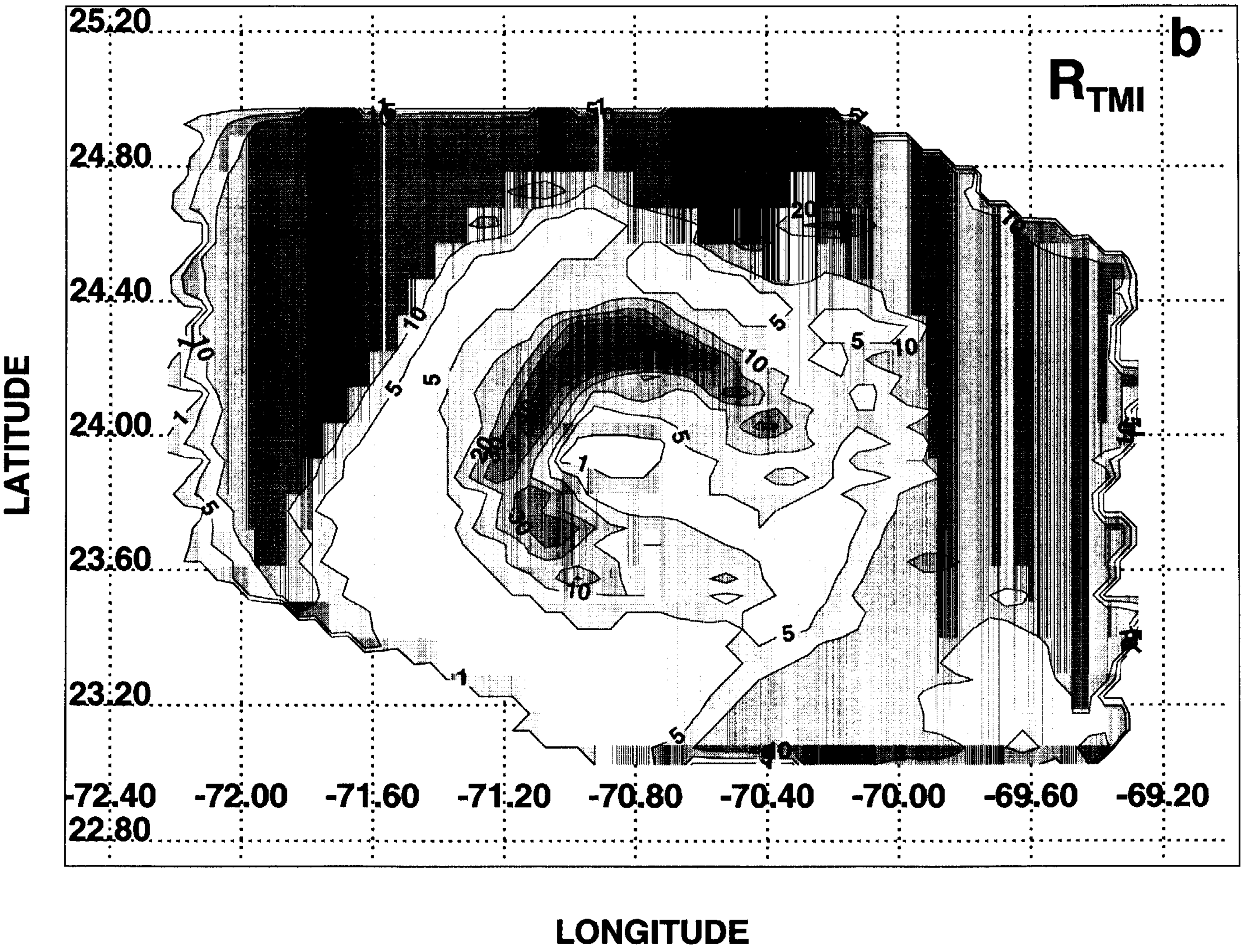
b
R_TMI
LATITUDE
25.20
24.80
24.40
24.00
23.60
23.20
22.80
LONGITUDE
-72.40
-72.00
-71.60
-71.20
-70.80
-70.40
-70.00
-69.60
-69.20
1
5
10
20
30

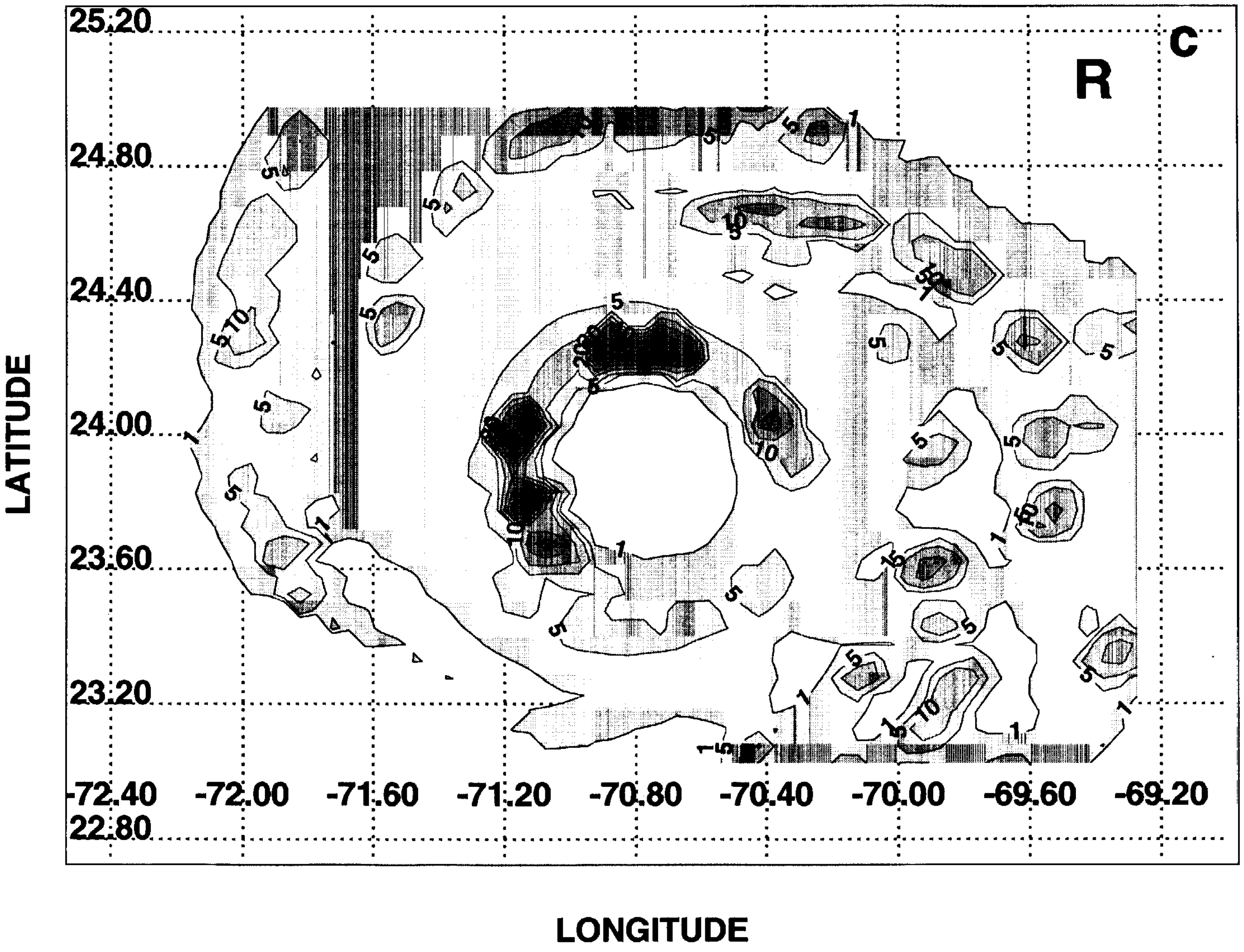
R
C
25.20
24.80
24.40
24.00
23.60
23.20
22.80
LATITUDE
-72.40
-72.00
-71.60
-71.20
-70.80
-70.40
-70.00
-69.60
-69.20
LONGITUDE
1
5
10
20

7c

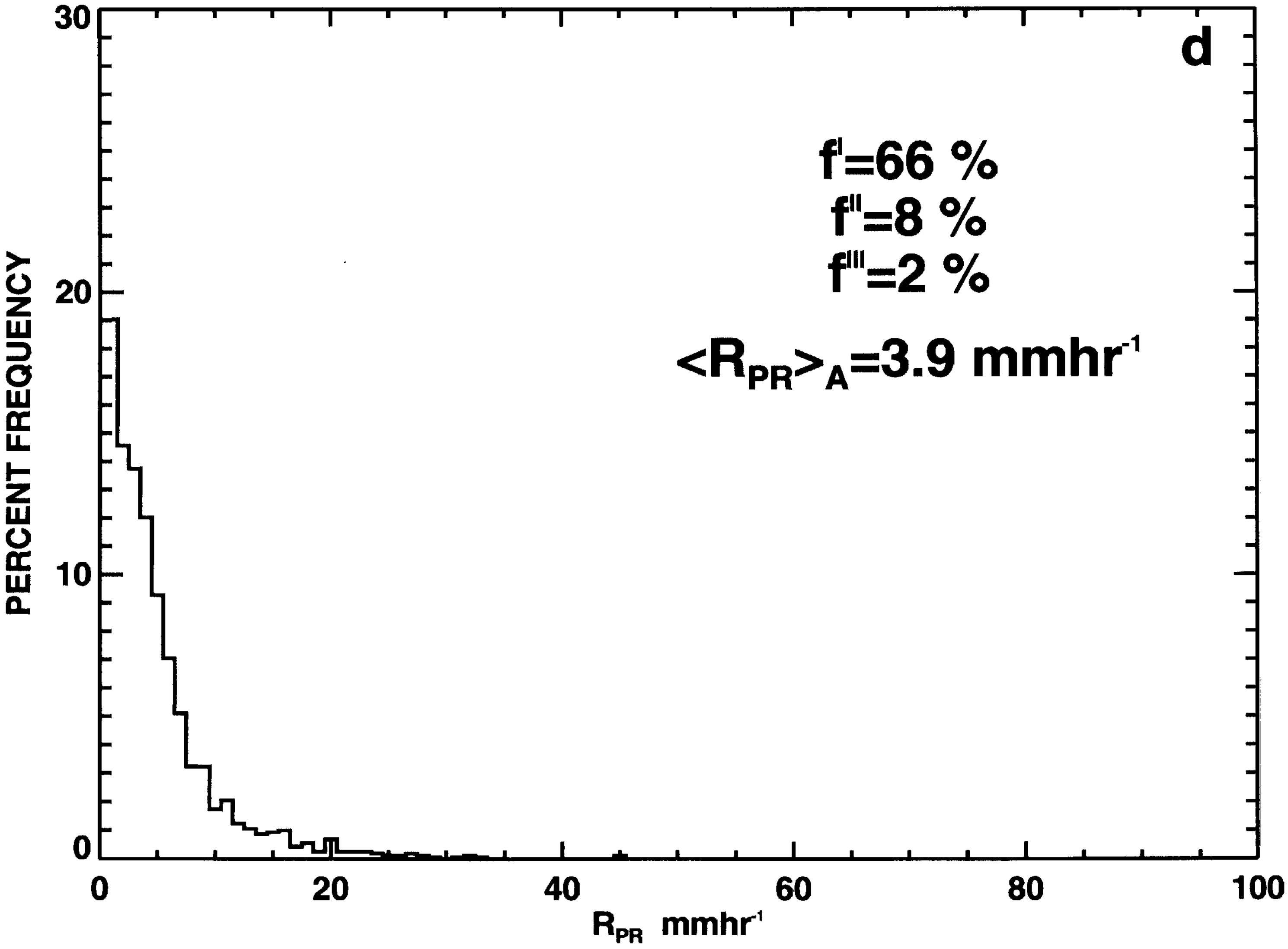
d
f^{I}=66 %
f^{II}=8 %
f^{III}=2 %
$\langle R_{PR}\rangle_A$=3.9 mmhr^{-1}
PERCENT FREQUENCY
0
10
20
30
0
20
40
60
80
100
R_{PR} mmhr^{-1}

PL

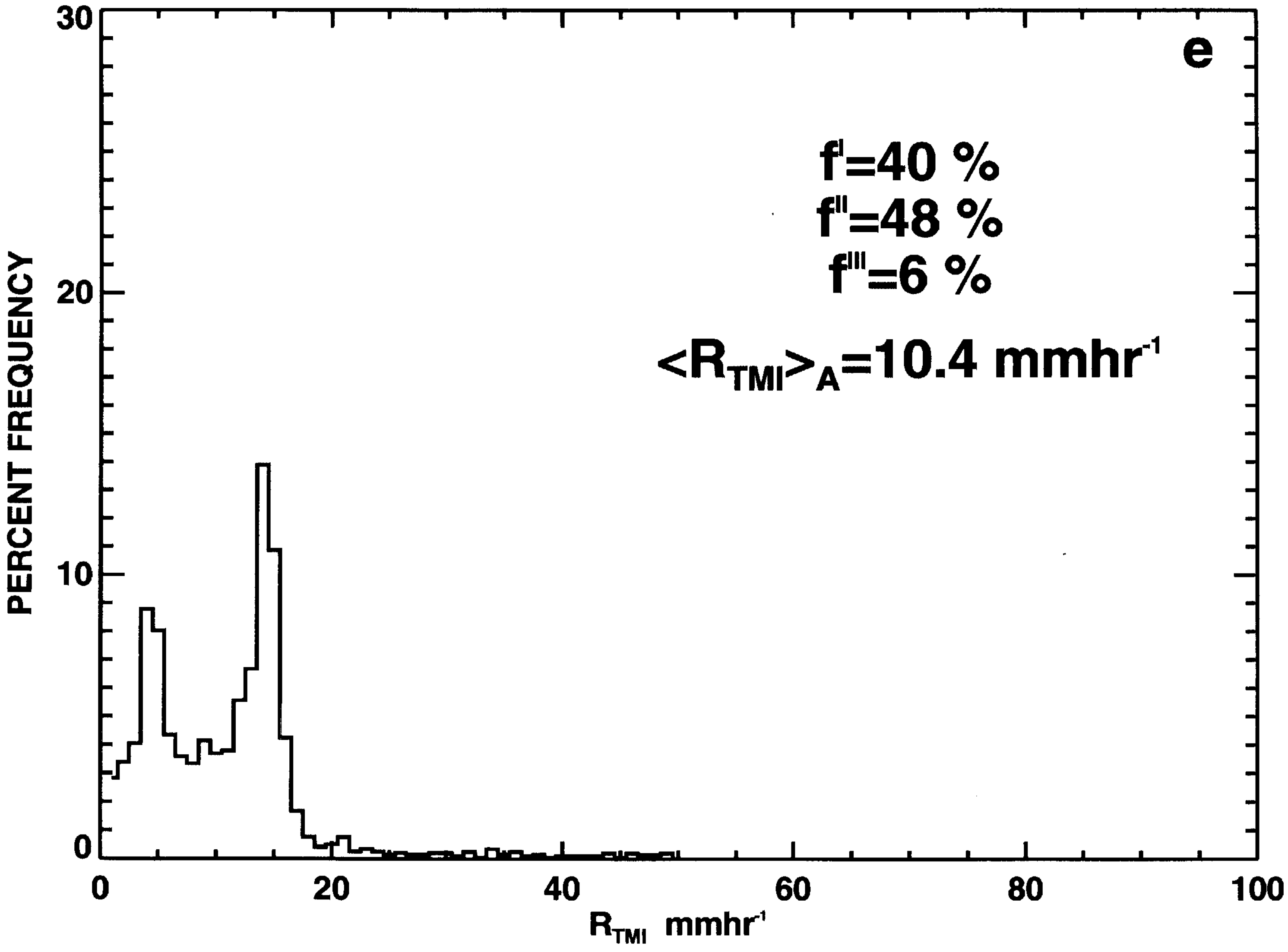
e
f^{I}=40 %
f^{II}=48 %
f^{III}=6 %
$\langle R_{TMI} \rangle_A$=10.4 mmhr^{-1}
PERCENT FREQUENCY
0
10
20
30
0
20
40
60
80
100
R_{TMI} mmhr^{-1}

7e

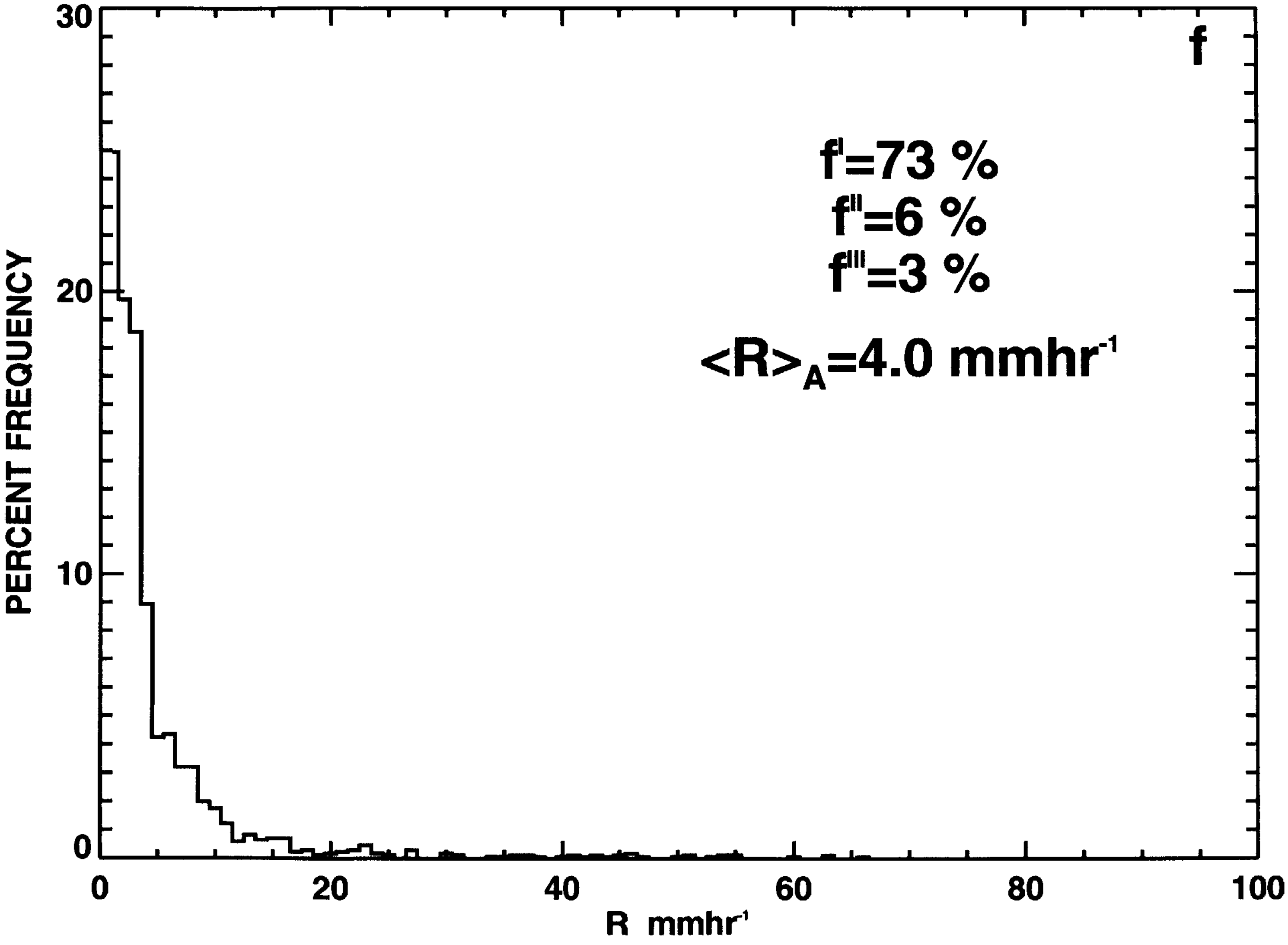
f
f' =73 %
f'' =6 %
f''' =3 %
<R>_A =4.0 mmhr^-1
PERCENT FREQUENCY
0
10
20
30
0
20
40
60
80
100
R mmhr^-1

7F

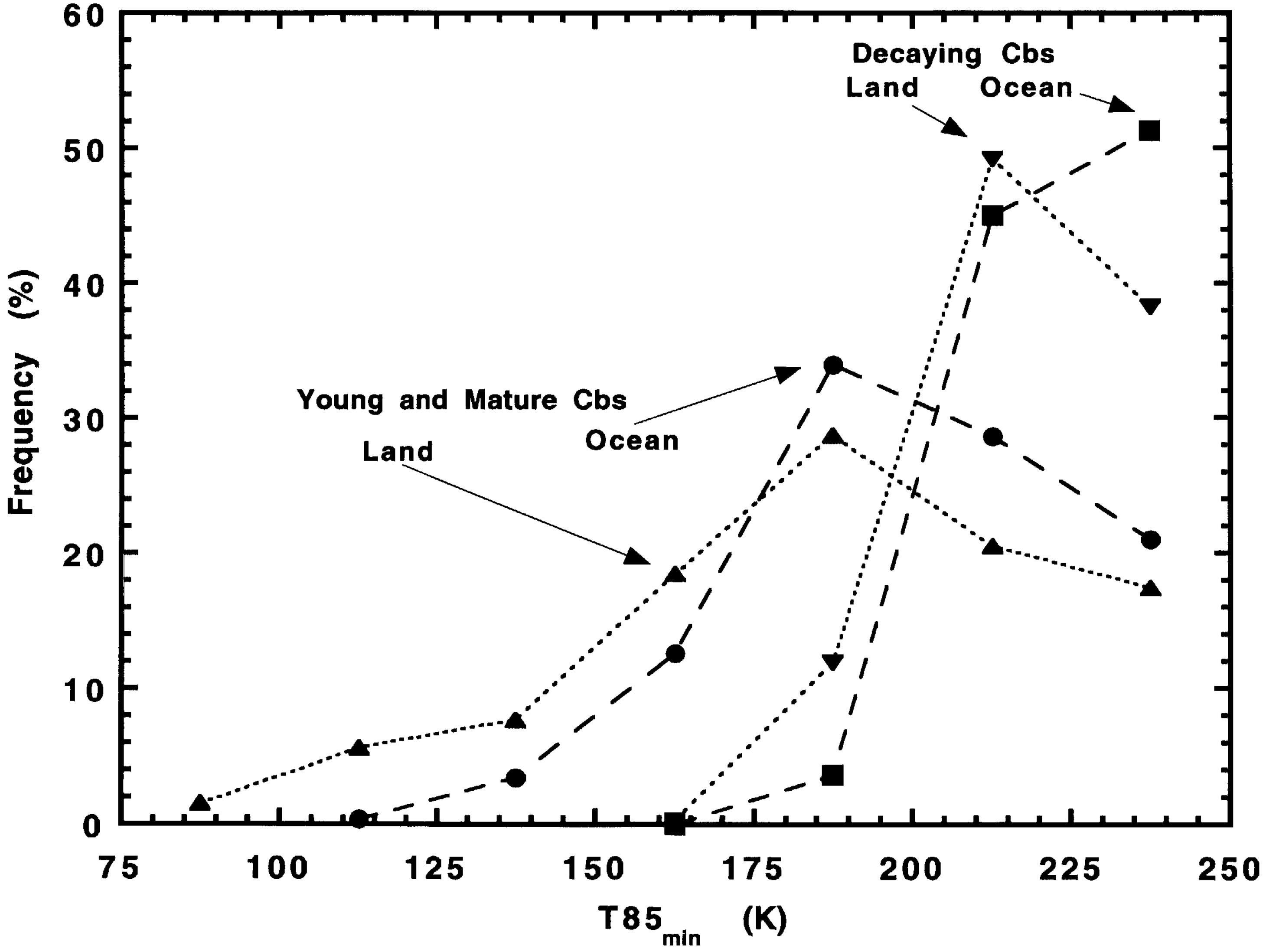
Decaying Cbs
Land
Ocean
Young and Mature Cbs
Land
Ocean
Frequency (%)
60
50
40
30
20
10
0
75
100
125
150
175
200
225
250
$T85_{min}$ (K)

8